Acoustic Meta-atoms: An Experimental Determination of the Monopole and Dipole Scattering Coefficients

Joshua Jordaan
U5351198

Supervised by Dr. David Powell

December 2017

A thesis submitted in part fulfilment of the degree of

Bachelor of Engineering
The Department of Engineering
Australian National University

This thesis contains no material which has been accepted for the award of any other degree or diploma in any university. To the best of the author's knowledge, it contains no material previously published or written by another person, except where due reference is made in the text.

Joshua Jordaan
3 December 2017

Acknowledgements

I'd like to thank my supervisor, Dr. David Powell for giving me the opportunity to undertake this project and introducing me to the fascinating world of metamaterials. The greatly appreciated advice, and at times much needed explanations he has provided throughout the year were instrumental in completing this thesis, and they have broadened my understanding of a topic I was completely new to only a year ago. I'd like to thank my friends Peter Atkinson and Ryan Bradley; the brules. Their support and company was always a big part of making the last five years of my degree the incredible experience they have been. Finally I would like to thank my parents and my amazing girlfriend Mel for all the ongoing support and motivation (and coffee).

Abstract

Acoustic metamaterials are materials engineered to manipulate and structure acoustic fields to a degree with no parallel in natural materials. They are created from small sub-wavelength sized unit building blocks referred to as meta-atoms. These are generally arranged in a periodic array to form what behaves as a continuous metamaterial. There are many potential applications of acoustic metamaterials all with novel properties not seen in other devices; such as cloaking, super-efficient sound absorbers and thin spatially compact acoustic lenses. Meta-atom scattering terms of monopolar and dipolar symmetry have been shown to relate to the effective bulk modulus and effective fluid mass density of a homogenised metamaterial. Where, taken together these parameters define the acoustic wave propagation through a material. Due to their importance in acoustic metamaterials, this thesis describes the development and implementation of a method to experimentally determine the monopole and dipole scattering coefficients of meta-atoms. To do this, an acoustic measurement apparatus is modified and characterised to ensure accurate two-dimensional acoustic field data can be obtained. A method of extracting the monopole and dipole scattering coefficients from recorded acoustic data is then defined. This method is based on fitting the experimental incident and scattered field data of meta-atoms to acoustic multipole expansions. The scattering coefficients of a rigid circular cylinder is then determined using the developed method, and found to agree well with analytical values. Better agreement is seen at frequencies over 1000 Hz, where experimental error from the measurement apparatus is reduced. Meta-atoms previously presented in the literature are also fabricated, and their scattering coefficients determined. These are found to agree with simulated values of monopolar and dipolar resonances also taken from the literature. Where, better agreement is again observed at resonances above 1000 Hz.

Contents

Acknowledgements i

Abstract ii

List of Figures viii

List of Abbreviations ix

1 Introduction 1
- 1.1 Overview of Metamaterials . . . 1
- 1.2 Overview of Acoustic Metamaterials (AMM) . . . 2
- 1.3 Resonant Meta-atoms, Metasurfaces and the Importance of Monopolar/Dipolar Scattering . . . 3
- 1.4 Previous Work in Experimental AMM . . . 5
- 1.5 Research Objective and Motivation . . . 7

2 Theory 9
- 2.1 The Acoustic Wave Equation . . . 9
- 2.2 The Multipole Scattering Coefficients of a 2D Rigid Circular Cylinder 11
- 2.3 The Multipole Scattering Coefficients of 2D Meta-atoms . . . 16
- 2.4 Summary . . . 19

3 Experimental Apparatus and Methods 21
- 3.1 Overview and Function of the Acoustic Field Measurement Apparatus 21
- 3.2 Characterisation and Modification of Measurement System . . . 23
  - 3.2.1 Mechanical control over microphone . . . 23
  - 3.2.2 Acoustic boundaries and parallel plate separation of waveguide 25
  - 3.2.3 Function and placement of loudspeaker . . . 27
  - 3.2.4 Characterisation of finalised acoustic measurement apparatus . 28
- 3.3 Method of Obtaining Acoustic Field Data . . . 29
- 3.4 Summary . . . 30

4 Data Analysis 31

4.1 Method of Extracting the Monopole and Dipole Scattering Coefficients from Experimental Data 31
4.2 Complex Linear Least Squares Fitting and Error Analysis 32
4.3 Verification of Extraction Method 33
4.4 Summary 36

5 Design, Fabrication and Characterisation of Meta-atoms 37
5.1 Selected Meta-atom Designs and Fabrication Methods 37
5.2 Determining the Acoustic Scattering Coefficients of Meta-atoms . . . 38
5.2.1 Meta-atoms presented in the literature 38
5.2.2 Modified meta-atom designs 42
5.3 Summary 45

6 Conclusions and Future Work 46
6.1 Conclusions 46
6.2 Suggestions for Future Work 47

Bibliography 48

List of Figures

1.1 Material design space of AMM for different values of effective fluid density ρ and bulk compressibility $C = 1/K$, which is the inverse of the bulk modulus defined in text. Here TA stands for transformation acoustics, which uses form invariant transformations of the acoustic wave equation to design materials which can arbitrarily shape sound, such as in cloaking devices [2]. Image taken from Haberman [9]. . . . 3

1.2 Left: AMM consisting of a periodic array of Helmholtz resonators and membranes to generate negative ρ_{eff} and K_{eff}, taken from Haberman [9]. Right: One of the first AMM consisting of metal and rubber meta-atoms in an epoxy resin. A close up of the meta-atom is shown (A) and the bulk metamaterial (B). Image taken from Liu et al. [16]. . . . 3

1.3 Examples of phase gradient style acoustic metasurfaces. Left: labyrinthine meta-atoms designed to control a reflected wave. Image taken from Li et al. [15]. Right: array of meta-atoms used to control a transmitted wave. Image taken from Xie et al. [28]. 5

1.4 (a) Layout of experimental apparatus used in [15] to record the 2D acoustic field of a metasurface. The edges shown are perfectly matched layer (PML) boundaries consisting of anechoic wedge shaped foam. (b) Image of 2D acoustic field measurement apparatus used in [30]. The microphone gantry arm and stepper motors are visible on top of the black parallel plate waveguide. 6

2.1 Plane wave with wave vector $\vec{k}$ offset by from the x-axis by angle θ_0 incident on a rigid circular cylinder of radius a. 12

2.2 Plots of the pressure field defined in (2.33) for $ka = 1$, $\theta_0 = 0$ and$t = 0$, truncated at 20th order terms. The circular cylinder the incident plane wave scatters off is shown in white, and the plane wave is incident from the left. 15

2.3 Plots showing the real part of the monopole, dipole and quadrupole terms ($n = 0, 1, 2$) in the multipole expansion of the plane wave given in (2.22) for $\theta_0 = 0$. 15

3.1 Top left: Diagram of acoustic measurement apparatus, showing the layout of components from above the parallel plate waveguide. The coordinate system convention used is in data analysis is also indicated. Top right: Side on and close up photograph of the waveguide with plates closed. The function of the microphone arm is indicated, showing the necessary gap to allow movement. Bottom: Close up of microphone sitting on top of perspex waveguide plate, it is glued to the driving belt. 22
3.2 Side on view of the entire acoustic field measurement apparatus with the top plate lifted to allow access to the test chamber. The main functional components are labelled. 22
3.3 Left: Amplitude of acoustic field where the effects of the stepper motor skipping are apparent. Right: Comparison of previous cable guide system and the current one installed as part of the solution to the stepper motor skipping problem. 24
3.4 Left: Labelling and measurements of each anechoic foam tested to minimise relfections from waveguide edges. The number of each foam is highlighted blue. Right: Reflection test results of each foam, with 0 cm being near the loudspeaker and ∼140 cm being as close to the acoustic boundary as possible. The amplitude is recorded in arbitrary units (a.u.), and the test acoustic frequency used was 2500 Hz. 25
3.5 a) Phase of acoustic field in waveguide using an external 9 cm diameter loudspeaker source. b) The amplitude of the same field measured in arbitrary units (a.u.). c) Phase of the acoustic filed using an internal 5 cm diameter loudspeaker. d) Amplitude of internal loudspeaker field. The acoustic frequency in all plots is 2250 Hz. 27
3.6 Top: Phase and amplitude of acoustic field in finalised measurement system at 2250 Hz. Bottom: Amplitude of acoustic field as a function of distance away from microphone (0 cm being closest), plotted for frequencies in the range 500 - 2500 Hz in 100 Hz increments. Amplitudes shown in arbitrary units (a.u.). 28

4.1 Diagram of the acoustic field measurement apparatus while performing a scan. The regions of the xy plane accessible to the microphone are labelled. 31
4.2 Left: Rigid cylinder scattering coefficients were extracted from. Right: Plots showing the normalised residuals of fitting the scattered and incident fields of the cylinder to (2.49) for various orders of n. 33

4.3 Results of extracting the monopole (α_0) and dipole (α_1) scattering coefficients of a 50 mm diameter rigid cylinder by fitting the experimental fields to (2.49) and comparing the results to (2.34). Error bars show $\pm 2\sigma$ in α_0 and α_1. 34
4.4 Examples of fitting the incident and scattered fields of a 50 mm diameter rigid cylinder to the multipole expansions in (2.49) to 10th order terms. The experimental and fitted fields are shown, as are the amplitude of the fields in arbitrary units and the phase in degrees. The acoustic field is incident from the bottom ($\theta_0 = \pi/2$) and the centre of the cylinder is situated at the origin. The acoustic frequency in all plots is 2000 Hz. 35

5.1 Diagrams of the meta-atom designs that were characterised. Meta-atom A was taken from [4], B from [17] and C and D modified versions of A. The diagram of meta-atom B defines the parameters wall thickness 't', channel width 'w' and meta-atom radius 'R'. For A: R = 50 mm, w = 4 mm and t = 1 mm B: R = 40 mm, w = 6 mm, t = 2 mm. C: R = 25 mm, w = 4 mm, t = 1 mm. D: R = 25 mm, w = 2 mm, t = 0.5 mm. 38
5.2 Fabricated meta-atoms, the diagrams of which are in Fig. 5.1. All meta-atoms were 3D printed using PLA plastic with a 0.1 mm layer thickness to a 66 mm height. 38
5.3 Top and middle: Results of extracting the scattering coefficients of meta-atom A. The zero crossings of the phase, associated with resonances have been indicated in red, for α_0 at 630 Hz, α_1 at 1220 Hz. Bottom left: Scattered field expansion coefficient $i\alpha_1$ for comparison with Fig. 5.4. Error bars correspond to a standard deviation in the error propagated from the fit parameters. Bottom right: Normalised residuals of fitting the scattered and incident fields. 39
5.4 Semi-analytically derived scattered field expansion coefficients of meta-atom A, taken from [4]. Here m represents the angular order of the coefficient. 40
5.5 Top and middle: Results of extracting the scattering coefficients of meta-atom B. The zero crossing of the phase associated with the resonance has been indicated in red, for α_0 at 1330 Hz. Error bars correspond to a standard deviation in the error propagated from the fit parameters Bottom: Normalised residuals of fitting the scattered and incident fields. 41

5.6 Top and middle: Results of extracting the scattering coefficients of meta-atom C. The zero crossing of the phase associated with resonance has been indicated in red, for α_0 at 2170 Hz. Error bars correspond to a standard deviation in the error propagated from the fit parameters Bottom: Normalised residuals of fitting the scattered and incident fields. 43

5.7 Top and middle: Results of extracting the scattering coefficients of meta-atom D. Some zero crossings of the phase can tentatively be observed to indicate resonance, these have been indicated in red, for α_0 at 925 Hz and α_1 at 580 Hz. Error bars correspond to a standard deviation in the error propagated from the fit parameters Bottom: Normalised residuals of fitting the scattered and incident fields. . . . 44

Glossary of Terms

AMM	Acoustic metamaterial/metamaterials
EM	Electromagnetic
2D	Two dimensions/dimensional
3D	Three dimensions/dimensional
IQ	In-phase and quadrature
A.u.	Arbitrary units

Chapter 1

Introduction

This thesis is chiefly concerned with the scattering coefficients of acoustic meta-atoms. As a topic, this sits within the field of acoustic metamaterials (AMM), which is itself a subset of the broader realm of metamaterials. This chapter will provide a brief introduction to the subject of metamaterials as a whole, and seek to motivate why specifically determining the monopole and dipole scattering coefficients of meta-atoms is useful to the field of AMM. Objectives of the thesis will also be discussed as will relevant previous work in experimental AMM.

1.1 Overview of Metamaterials

The name metamaterials was coined by early pioneers of the field and is derived from the greek *meta*, meaning beyond; implying a class of materials which in some way go beyond conventional materials [2]. In general a metamaterial is any material that has been designed to produce properties that has no naturally occurring equivalent. In practice, most metamaterials are macroscopic composites that derive their unique properties from their carefully engineered structure and composition [30]. These structures are typically (but not necessarily) periodic and composed of small, sub-wavelength sized meta-atoms that in the bulk behave as a continuous material with unusual effective properties. Here 'meta-atom' refers to the unit-cell, or singular building block that a homogenisation scheme is applied to so that the effective properties of the bulk metamaterial can be derived. The first true metamaterial was made in 2000 and consisted of an array of sub-wavelength meta-atoms composed of copper split-ring resonators and wire elements deposited onto a circuit board substrate. It was engineered to produce an effective negative refractive index for microwave frequency electromagnetic (EM) waves [24]. This was a phenomenon which had only been theorised to exist, and which allowed for many un-before seen applications such as the creation of super-resolution lenses that surpass the diffraction limit [24]. Since their inception, the type and variety of metamaterials has grown to include acoustic, elastodynamic and mechanical; with applications span-

ning multiple domains such as holography, cloaking devices, enhanced photovoltaics, earthquake protection and focused ultrasound surgery [2, 29, 6].

1.2 Overview of Acoustic Metamaterials (AMM)

In AMM the governing equation is the scalar acoustic wave equation (see chapter 2)

$$\frac{\partial^2 p}{\partial t^2} - \frac{K}{\rho}\nabla^2 p = 0, \tag{1.1}$$

where p is the acoustic pressure, ρ the fluid mass density and K the bulk modulus. Here the key parameters that control wave propagation are K and ρ, and so these are the main properties of interest when designing AMM. In naturally occurring materials K and ρ are defined by the materials chemical composition and are always positive [6]. To go 'beyond' these natural materials involves creating negative or near zero values for K and ρ, which is a goal of AMM. The implications of negative or zero values for these parameters can be understood by examining how they effect wave propagation. For an acoustic wave travelling with wave vector $\vec{k}$, and frequency ω, the magnitude of $\vec{k}$ and index of refraction n are given by [13]

$$k = n\omega, \quad n = \sqrt{\rho/K}. \tag{1.2}$$

If we now imagine a scenario where the wave is propagating under a regime where effective values of ρ or K are negative, then we find that the phase velocity $v_p = k/\omega$ is purely imaginary which corresponds to exponential decay of the wave and opaque materials. In the case that $\rho \approx 0$ we can obtain a media that can transmit sound with very little distortion and zero phase change along its length [6]. For the interesting case where both the effective ρ and K are negative, it has been shown that n becomes negative [13] and the incident sound wave refracts in the opposite direction to conventional materials, which as in the case of EM metamaterials can be used to produce acoustic super-lenses and sub-wavelength imaging devices [6]. In Fig. 1.1 a diagram shows the material design space for AMM and gives some further examples of the type of applications possible.

Figure 1.1: Material design space of AMM for different values of effective fluid density ρ and bulk compressibility $C = 1/K$, which is the inverse of the bulk modulus defined in text. Here TA stands for transformation acoustics, which uses form invariant transformations of the acoustic wave equation to design materials which can arbitrarily shape sound, such as in cloaking devices [2]. Image taken from Haberman [9].

1.3 Resonant Meta-atoms, Metasurfaces and the Importance of Monopolar/Dipolar Scattering

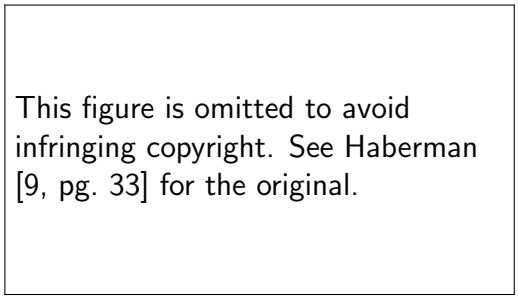

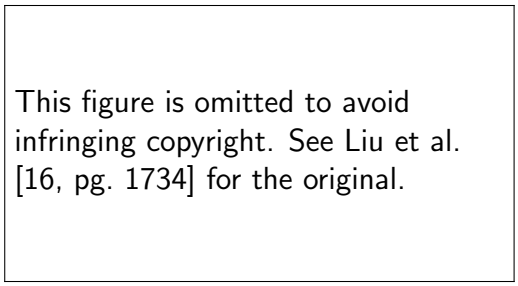

Figure 1.2: Left: AMM consisting of a periodic array of Helmholtz resonators and membranes to generate negative ρ_{eff} and K_{eff}, taken from Haberman [9]. Right: One of the first AMM consisting of metal and rubber meta-atoms in an epoxy resin. A close up of the meta-atom is shown (A) and the bulk metamaterial (B). Image taken from Liu et al. [16].

One method of accessing the design space of Fig. 1.1 is by constructing AMM from resonant meta-atoms. These typically generate negative effective mass density (ρ_{eff}) or bulk modulus (K_{eff}) when the incident field acts as a driving term at frequency just above resonance [13]. Under these circumstances the negative effective para-

meters are a dynamic effect and are often referred to as dynamic bulk modulus/mass density [22]. One simple resonant structure that exhibits $-\rho_{eff}$ consists of a tube with membranes fixed to the ends [6]. The fluid inside behaves like a driven mass spring system and can experience oscillations 180° out of phase with the driving term, whereby it accelerates in the opposing direction of the applied force hence achieving $-\rho_{eff}$. Similar structures can be used to produce $-K_{eff}$. These consist of closed cavities connected to a waveguide via a narrow channel to form Helmholtz resonators [6]. Just above the cavities natural frequency the resonator acts as a dynamic volume source allowing for volume expansion under a compressive load; producing $-K_{eff}$. Carefully designed combinations of these structures can produce both $-\rho_{eff}$ and $-K_{eff}$ over some frequency band. An example of this type of AMM is shown in Fig. 1.2. Although these are some of the simplest resonant meta-atom systems to conceptualise many more exist in the literature [5, 17, 16], and the most relevant to this thesis are of form of spherical or cylindrical scatterers. These are generally studied in the long wavelength limit, where most inhomogeneities can be approximated by an effective medium description of spherical/cylindrical inclusions with acoustic scattering dominated by Mie-type monopole and dipole terms [13]. In this instance it has been found that the symmetric expansion/contraction associated with monopolar meta-atom modes gives rise to a resonant response of K_{eff}, whereas the antisymmetry of dipolar modes create a resonant response in ρ_{eff} [13]. Higher order modes have been shown to have interesting effects in elastodynamic materials [18], but have not been directly associated with useful design parameters in AMM. One of the first AMM ever made used this scheme. It was created from a cubic lattice array of sub-wavelength scale meta-atoms with overlapping dipole and monopole resonances, enabling simultaneous negative ρ_{eff} and K_{eff}. The meta-atoms consisted of a metal sphere coated with a soft rubber and were embedded into an epoxy matrix [16]. An image of this AMM is also given in Fig. 1.2.

Another type of AMM are acoustic metasurfaces. These are characterised as having a sub-wavelength thickness and can produce much of the complex acoustic field manipulations as bulk AMM but in a highly spatially compact form [29]. They can be made from resonant meta-atoms [29, 4] but are also associated with labyrinthine structures that make use of the generalised Snell's law to generate a phase gradient along the surface to shape the acoustic wavefront [15]. Their principle of operation is that the acoustic field propagates through the narrow sub-wavelength passages of the structure with very little distortion [23]. The winding meta-atom structure then allows for a full 0 to 2π phase shift via changing some design parameter such as the number of windings or the width of the channels [23]. This then allows the phase gradient needed to produce the desired output wavefront, to be discretised

and implemented with an array of the phase shifting meta-atoms. An example of a reflecting and transmitting metasurface generated in this way is given in Fig. 1.3.

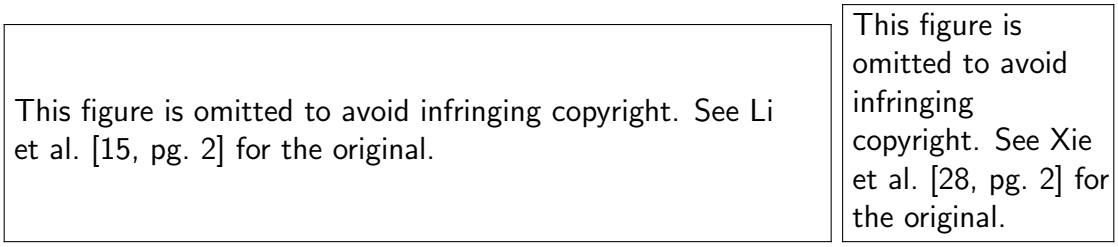

Figure 1.3: Examples of phase gradient style acoustic metasurfaces. Left: labyrinthine meta-atoms designed to control a reflected wave. Image taken from Li et al. [15]. Right: array of meta-atoms used to control a transmitted wave. Image taken from Xie et al. [28].

These labyrinthine acoustic metasurfaces have been shown to exhibit excellent wavefront shaping potential [15, 23, 29]. However, recent research has found that using the generalised Snell's law alone to design the phase gradient imposes fundamental limitations on the energy efficiency of the transmitted or reflected wavefront; with some energy always lost to undesired directions even for lossless metasurfaces [7]. It was found that in the case of transmitted waves, in order to realise full control over acoustic energy flow a local and non-symmetric acoustic response of the meta-atoms is required [7]. In acoustic meta-atoms it has been shown that this non-symmetric response equates to the coupling of the ρ_{eff} and K_{eff} parameters [22], which in turn relates to the coupling of the monopolar and dipolar scattering terms [13].

1.4 Previous Work in Experimental AMM

There have been numerous experimental studies in acoustic metamaterials and acoustics in general which are of relevance to the experimentation carried out in this thesis. As the acoustic fields considered here were collected inside of a parallel plate waveguide (see chapter 3) they are exclusively 2D, so that previous work in 2D acoustics is especially pertinent. When designing and testing AMM a 2D regime is often preffered due to the reduction in complexity and ease of acoustic field recording it affords. This is especially true in the case of metasurfaces as their geometry lends itself to a 2D design method.

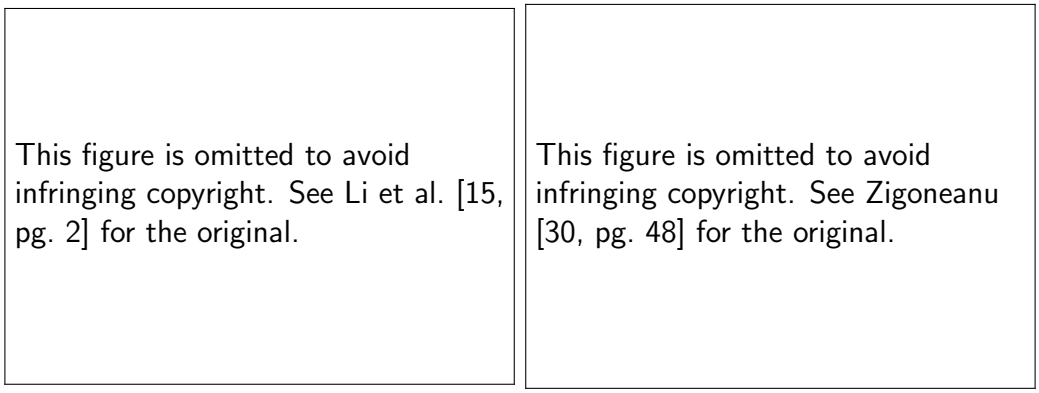

(a) **(b)**

Figure 1.4: (a) Layout of experimental apparatus used in [15] to record the 2D acoustic field of a metasurface. The edges shown are perfectly matched layer (PML) boundaries consisting of anechoic wedge shaped foam. (b) Image of 2D acoustic field measurement apparatus used in [30]. The microphone gantry arm and stepper motors are visible on top of the black parallel plate waveguide.

When testing a reflective metasurface Li et al. [15] successfully used the experimental apparatus shown in Fig. 1.4a. It consisted of a parallel plate waveguide (1.2 m $\times$ 1.5 m) into which the sample was placed. The edges of the waveguide were insulated using anechoic wedge shaped foam to minimise reflections back into the waveguide, and the spacing of the plates was 2.1 cm. A 30 mm diameter loudspeaker was placed outside but very near the top of the waveguide, and propogated sound into the chamber via a 20 mm diameter hole cut into the top plate. They recorded the field inside of the chamber by using two microphones. One was a reference microphone fixed near the loudspeaker opening, and the other was moveable and scanned the 2D field in the region indicated. The relative phase and magnitude of the field was retrieved by analysing the cross spectrum of the two microphones, and the scattered field was taken as the difference between the incident field recorded in an empty chamber and the total field recorded with the metasurface. The parallel plate waveguide used ensures a 2D propagating wave so long as higher order modes are not supported between the plates. This leads to a cut-off frequency f_c of $f_c = c/2d$ where c is the velocity of sound and d is the separation of the plates. For the waveguide in [15] the 2.1 cm separation gives a cut-off of 8.17 kHz. Although Li et al. [15] report accurate 2D field measurements, a limitation of their paper is that they do not discuss further details as to the microphone movement system and the exact type of anechoic foam used. However, the general approach shown of using a waveguide to ensure 2D sound propagation, a scanning microphone set-up, and an analysis of the cross spectrum with a reference microphone to record the phase and magnitude of the field appears to be exemplary of the approach used by many others in the field with very similar apparatus successfully used in [23, 27, 31, 28]. Another more detailed example of this type of 2D acoustic field measurement

apparatus was presented in Zigoneanu [30], and is shown in Fig. 1.4b. Here the author used a 1.2 m^2 parallel plate waveguide, with a 5.08 cm plate separation giving a cut-off of 3.38 kHz. The waveguide also had anechoic foam edging in the form of wedge shaped foam. The loudspeaker was placed inside of the waveguide, and the field recorded using a reference and scanning microphone. The author also explicitly describes that the mechanism for moving the second microphone is through two stepper motors controlled via an interface with MATLAB software on a PC, where the microphone itself is attached to a gantry arm to move in the xy plane. Unfortunately none of the studies presented above give any detail about the exact type of wedge shaped anechoic foam used beyond a cursory description. Fortunately, other work in acoustics has investigated the use of different foams. A study by Beranek and Sleeper [3] on the design and construction of anechoic chambers found an optimal anechoic foam design they titled the 'harvard linear wedge'. This was created from an open-cell foam and had a wedge that was 80% of the foams total thickness and a wedge tip angle of 11.2°. Additionally, a slightly contradictory study by Kang and Bolton [12] found that in the explicitly 2D case, keeping the wedge 80% of the foams thickness but using a broader wedge tip of 36% was optimal. Taken together these results fully describe the type and function of the acoustic field measurement apparatus most commonly used to record 2D field when studying AMM.

1.5 Research Objective and Motivation

AMM offer powerful new ways of manipulating acoustic fields for a variety of applications. These include cloaking, efficient sound absorbers, spatially compact imaging devices and more generally arbitrary control over an acoustic wavefront [6, 8, 24]. Mie-type monopolar and dipolar resonant meta-atoms play an important role in AMM, being one of the first types of meta-atom designs they have since been used to create a variety of metasurfaces and bulk AMM with novel properties such as negative refractive index, near-zero refractive index and very high absorption [4, 14, 18]. Furthermore, it has been found that creating a local non-symmetric response of meta-atoms would improve the performance of existing transmissive metasurfaces [7], an effect which may be realised by accessing the monopolar and dipolar scattering terms [22]. Clearly the acoustic monopole/dipole scattering coefficients of meta-atoms have a significant importance in the field of AMM, but to date have not been experimentally measured; with most designs relying on simulations or indirect observations of resonances attributed to the monopolar and dipolar modes [4, 14]. This thesis aims to address this gap in the literature by experimentally determining

the monopole and dipole scattering coefficients of acoustic meta-atoms. To achieve this aim, there are three main objectives: 1. Modify and characterise an existing 2D acoustic field measurement apparatus to ensure accurate data can be recorded. 2. Develop a method of extracting the monopole and dipole scattering coefficients, and verify the method by comparison with the analytical scattering coefficients of a rigid cylinder. 3. Successfully apply this method to determine the scattering coefficients of a meta-atom design presented in the literature.

Chapter 2

Theory

This chapter will present the relevant acoustic theory used in this thesis, starting with a derivation of the acoustic wave equation. The scattering problem of a 2D rigid cylinder will then be solved, and the analytical monopole and dipole scattering coefficients of the cylinder defined for later comparison in chapter 4. The general acoustic multiple expansion will also be described and applied to determine the scattering coefficients of arbitrary 2D geometries, which forms the basis of the meta-atom scattering coefficient extraction method defined in chapter 4.

2.1 The Acoustic Wave Equation

Consider an isotropic and homogeneous fluid described by scalar pressure and density fields p and ρ, and velocity vector field $\vec{u}$. Here the fluid is modelled as a continuum and these fields represent average values for some infinitesimal volume of the fluid. As we are interested only in fluctuations in the fluid due to some disturbance from an equilibrium position, these fields further represent only the difference in the fluid from it's equilibrium pressure, density and velocity.

The total rate of change of some property F of the fluid from a time t to $t + dt$ is given by

$$\frac{dF}{dt} = \frac{\partial F}{\partial t} + \vec{u} \cdot \nabla F \tag{2.1}$$

where the second term takes into account that the infinitesimal fluid volume element moves by a distance $\vec{u}dt$ during the time slice. The linear acoustic approximation will now be taken in deriving the acoustic wave equation, in that the spatial variation of a fluid property ∇F is neglected in comparison with the time variation $\partial F/\partial t$. The consequence of this simplification is that non-linear effects such as overmodulation of the medium are not accounted for [21].

The net particle flux through a surface S, enclosing a volume V can be related to

the divergence of the momentum via Guass's law

$$\int_S (\rho\vec{u}) \cdot d\vec{a} = \int_V \nabla \cdot (\rho\vec{u}) dV, \tag{2.2}$$

where $\vec{a}$ is the unit normal vector of surface S. This in turn is equal to the rate of mass lost from V, which gives

$$\int_V \nabla \cdot (\rho\vec{u}) dV = -\frac{d}{dt}\int_V \rho dV = -\int_V \frac{\partial}{\partial t}\rho dV. \tag{2.3}$$

As this must hold for arbitrary V the two integrands are equal; resulting in a statement of conservation of mass in a fluid, or the continuity equation

$$\nabla \cdot (\rho\vec{u}) = -\frac{\partial \rho}{\partial t}. \tag{2.4}$$

If a pressure gradient is present in the fluid, it results in a force causing the fluid to flow towards the region of low pressure. Using Newton's second law, mathematically this is

$$\nabla p = -\frac{\partial}{\partial t}(\rho\vec{u}). \tag{2.5}$$

Furthermore if a region of the fluid undergoes expansion, that region experiences a decrease in pressure proportional to the incompressibility, or bulk modulus K of the fluid. As the expansion rate is given as the divergence of the fluid velocity, the rate of change of the pressure is then given by

$$\frac{\partial p}{\partial t} = -K\nabla \cdot \vec{u}. \tag{2.6}$$

If we now take the divergence of both sides of (2.5) and substitute (2.6) we get

$$\nabla \cdot \nabla p = -\frac{\partial}{\partial t}\nabla \cdot (\rho\vec{u}) = \frac{\rho}{K}\frac{\partial^2 p}{\partial t^2}. \tag{2.7}$$

Denoting ∇^2 as the Laplacian operator results in the acoustic wave equation for the pressure field

$$\frac{\partial^2 p}{\partial t^2} = \frac{K}{\rho}\nabla^2 p = c^2\nabla^2 p, \tag{2.8}$$

where the speed of the wave $c = \sqrt{K/\rho}$. From the continuity equation (2.4) it appears that in the case of a compressible fluid (such as air), the volume changes associated with a propagating acoustic wave result in a density field implicitly dependant on pressure. This complexity however, can be removed by using the definition of

the bulk modulus [19].

$$K = -V\frac{dp}{dV}. \tag{2.9}$$

It has been experimentally shown that the rapid pressure changes occurring in acoustic wave propagation in a compressible fluid do not exchange heat with their surroundings and are hence adiabatic [19]. For adiabatic processes in an ideal gas pV^γ is a constant, where $\gamma = C_p/C_v$ is the ratio of heat capacities at a specific pressure and volume. Putting this relationship into (2.9) gives the general result

$$K = \gamma p \tag{2.10}$$

for adiabatic processes. Now using the ideal gas law $p = \rho RT$, where R is the specific gas constant of the fluid and T is the absolute temperature, we find

$$\rho = \frac{p}{RT}. \tag{2.11}$$

Substituting (2.10) and (2.11) into (2.8), results in an acoustic pressure wave speed for a compressible fluid of

$$c = \sqrt{\gamma RT}, \tag{2.12}$$

which is only dependent on material constants. In dry air at 20 ℃ this speed has been measured to be about 343 m/s [11].

2.2 The Multipole Scattering Coefficients of a 2D Rigid Circular Cylinder

Having defined the acoustic wave equation, the problem of acoustic scattering from an object can now be approached. This section will derive the scattering coefficients of a 2D rigid circular cylinder and introduce relevant 2D acoustic scattering theory.

In 2D the simplest scattering problem is that of a plane wave of wave vector $\vec{k}$ incident on a rigid circular cylinder of radius a which is of infinite length in the out of plane direction. A diagram of this is given in Fig. 2.1 below.

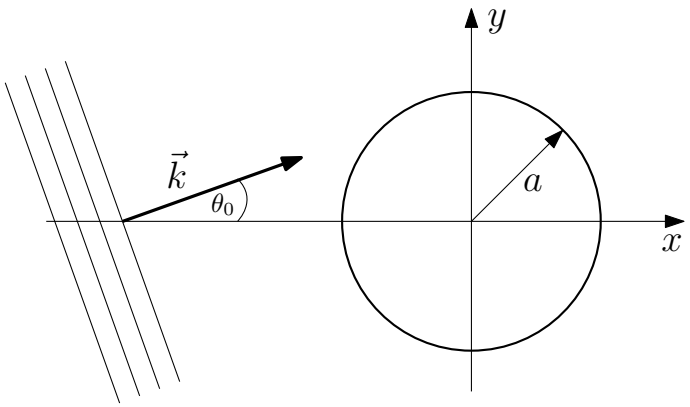

Figure 2.1: Plane wave with wave vector $\vec{k}$ offset by from the x-axis by angle θ_0 incident on a rigid circular cylinder of radius a.

The time dependant acoustic pressure field over the domain can be written as

$$P(x, y, t) = \mathrm{Re}[p(x, y)e^{-i\omega t}] \tag{2.13}$$

where frequency $\omega = kc$ and k is the wave number, such that using (2.8) we find $p(x, y)$ is subject to the Helmholtz equation

$$\nabla^2 p + k^2 p = 0. \tag{2.14}$$

The total pressure amplitude p is equal to the sum of the incident and scattered waves

$$p = p_I + p_S \tag{2.15}$$

where the incident plane wave is

$$p_I = p_0 e^{i\vec{k}\cdot\vec{r}}, \tag{2.16}$$

with implicit harmonic time dependence from (2.13). Here $\vec{r}$ is a position vector from the origin located at the centre of the cylinder as shown in Fig. 2.1. The radial symmetry of the scattering problem lends itself to polar coordinates, where r is the radial distance from the origin and θ the angle from the x-axis. The plane wave can now be re-written using θ_0 as the angle of incidence of the plane wave with respect to the x-axis, such that we get

$$\vec{k} = k(\cos\theta_0, \sin\theta_0), \quad \vec{r} = r(\cos\theta, \sin\theta) \tag{2.17}$$

which gives

$$p_I = p_0 \exp[ikr(\cos\theta_0 \cos\theta + \sin\theta_0 \sin\theta)] = p_0 e^{ikr\cos(\theta-\theta_0)}. \tag{2.18}$$

The key aspect to solving this scattering problem is to perform a partial wave expansion of the incident plane wave. This will proceed as follows. Let $\phi = \theta - \theta_0$, such that it is clear $e^{ik\cos\phi}$ is periodic in ϕ and can be expanded in terms of a Fourier series,

$$e^{ikr\cos\phi} = \sum_{n=-\infty}^{\infty} c_n e^{in\phi} \tag{2.19}$$

where

$$c_n = \frac{1}{2\pi}\int_0^{2\pi} e^{ikr\cos\phi}e^{-in\phi}d\phi = \frac{1}{2\pi}\int_0^{2\pi} e^{ikr\cos\phi}[\cos n\phi - i\sin n\phi]d\phi. \tag{2.20}$$

As $e^{ik\cos\phi}$ is even in ϕ the sine term goes to zero such that

$$c_n = \frac{1}{2\pi}\int_0^{2\pi} e^{ikr\cos\phi}\cos n\phi d\phi = \frac{1}{\pi}\int_0^{\pi} e^{ikr\cos\phi}\cos n\phi d\phi = i^n J_n(kr), \tag{2.21}$$

where the last equality is found using a standard integral representation of the Bessel function of the first kind, $J_n(z)$ [20]. Applying this to (2.19) gives

$$e^{ikr\cos(\theta-\theta_0)} = \sum_{n=-\infty}^{\infty} i^n J_n(kr)e^{in(\theta-\theta_0)}. \tag{2.22}$$

so we finally get

$$p_I = p_0 e^{ikr\cos(\theta-\theta_0)} = p_0\sum_{n=-\infty}^{\infty} i^n J_n(kr)e^{in(\theta-\theta_0)}. \tag{2.23}$$

Each term in the plane wave expansion series represents a distinct angular variation and is known as a partial wave. Having described the incident field as a partial wave expansion in polar coordinates, we can now turn to the scattered field. Using separation of variables, the scattered field is represented as

$$p_S = R(r)\Theta(\theta). \tag{2.24}$$

Applying the Helmholtz equation (2.14) to p_S gives

$$r^2R'' + rR' + (k^2r^2 - n^2)R = 0, \quad \Theta'' + n^2\Theta = 0 \tag{2.25}$$

where $n \in \mathbb{Z}$ are integer eigenvalues so that Θ is periodic in θ. The most general

solutions to (2.25) are

$$\Theta_n = A_n e^{in\theta} + B_n e^{-in\theta}, \quad R_n = C_n H_n^{(1)}(kr) + D_n H_n^{(2)}(kr) \tag{2.26}$$

where $H_n^{(1)}$ and $H_n^{(2)}$ are Hankel functions of the first and second kind. As $r \to \infty$, p_S must be an outgoing wave, to satisfy the radiation condition of the scattered field. Due to fact that in the far field $H_n^{(2)}$ behaves as incoming radiation [20], D_n is immediately set to zero, leaving

$$p_S = \sum_{n=-\infty}^{\infty} (A_n e^{in\theta} + B_n e^{-in\theta})(C_n H_n(kr)) \tag{2.27}$$

where $H_n^{(1)}$ will be denoted as H_n from now on. At the surface of an acoustically hard surface the fluid velocity component normal to the surface must be zero. Using the conservation of momentum relationship in (2.5) this results in the Neumann boundary condition at the surface of the cylinder:

$$\frac{\partial p_I}{\partial r} + \frac{\partial p_S}{\partial r} = 0, \quad r = a. \tag{2.28}$$

Applying this to (2.27) and (2.23) gives

$$kC_n H_n'(ka)(A_n e^{in\theta} + B_n e^{-in\theta}) = -kp_0 i^n J_n'(ka) e^{in(\theta-\theta_0)}. \tag{2.29}$$

Without loss of generality, we can now set the angle of incidence to zero $\theta_0 = 0$, and $B_n = 0$ so that

$$G_n k H_n'(ka) e^{in\theta} = -kp_0 i^n J_n'(ka) e^{in\theta}. \tag{2.30}$$

Where the unknown coefficients are multiplied into G_n, which is found to be

$$G_n = -p_0 i^n \frac{J_n'(ka)}{H_n'(ka)} \tag{2.31}$$

So we get a scattered pressure wave

$$p_S = -p_0 \sum_{n=-\infty}^{\infty} i^n \frac{J_n'(ka)}{H_n'(ka)} H_n(kr) e^{in(\theta-\theta_0)}, \tag{2.32}$$

where the angle of incidence has been re-introduced as a simple coordinate translation. This gives a total time dependent pressure field of

$$P(r,\theta,t) = \mathrm{Re}\left[p_0 e^{-i\omega t} \sum_{n=-\infty}^{\infty} i^n \left(J_n(kr) - \frac{J_n'(ka)}{H_n'(ka)} H_n(kr) \right) e^{in(\theta-\theta_0)} \right] \tag{2.33}$$

In Fig. 2.2 below, a plot of the total pressure field at time $t = 0$, for $ka = 1$ is shown truncated at $n = \pm 20$ terms, along with a plot of the amplitude of the total field.

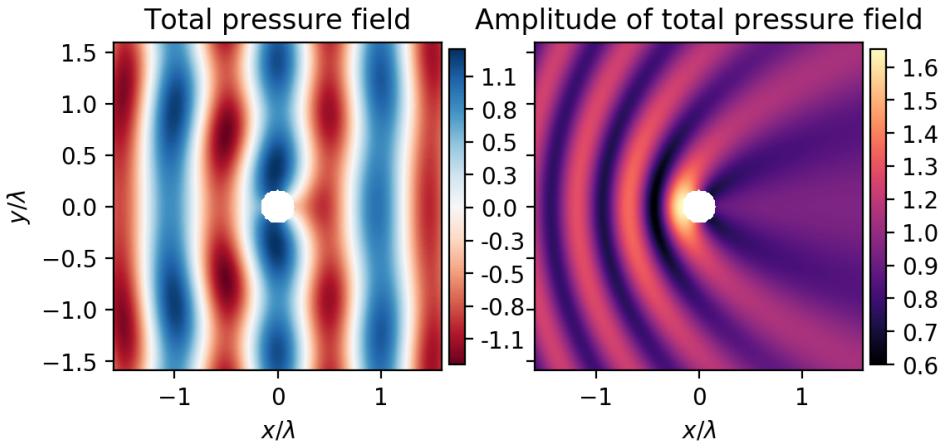

Figure 2.2: Plots of the pressure field defined in (2.33) for $ka = 1$, $\theta_0 = 0$ and$t = 0$, truncated at 20th order terms. The circular cylinder the incident plane wave scatters off is shown in white, and the plane wave is incident from the left.

The benefit of the partial wave expansion, is that the field due to distinct angular variations is immediately obtained. The $n = 0$ term is called the acoustic monopole, the $n = 1$ term the dipole, $n = 2$ the quadrapole and so on. More generally this type of solution to the Helmholtz equation in distinct angular and radial components is known as a multipole expansion [20] and due to it's role in Mie scattering theory in EM, resonances of the partial wave terms are often referred to as Mie-type in the field of AMM [18]. As an example of the angular and radial dependence of individual multipole terms, the real part of the $n = 0, 1, 2$ terms of the plane wave multipole expansion are given below in Fig. 2.3.

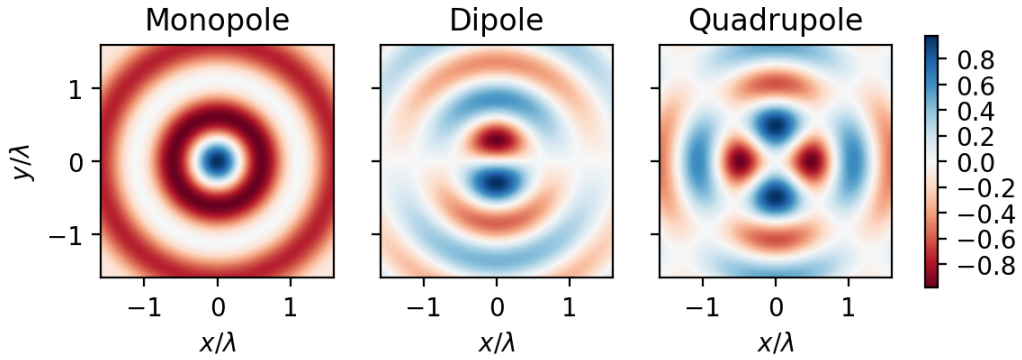

Figure 2.3: Plots showing the real part of the monopole, dipole and quadrupole terms $(n = 0, 1, 2)$ in the multipole expansion of the plane wave given in (2.22) for $\theta_0 = 0$.

We can now determine the multipole scattering coefficients of the rigid 2D cylinder by using the multipole expansions of the scattered and incident fields given in (2.32)

and (2.23) respectively. So, ignoring the spatial dependency of (2.32) and (2.23) we can write

$$\begin{aligned} \vec{p_S} &= \sum_{n=-\infty}^{\infty} (-p_0) i^n \frac{J_n'(ka)}{H_n'(ka)} = \alpha \cdot \vec{p_I} = \sum_{n=-\infty}^{\infty} \alpha_n p_0 i^n \\ \Rightarrow \ \alpha_n &= -\frac{J_n'(ka)}{H_n'(ka)}, \end{aligned} \tag{2.34}$$

where α_n is the scattering coefficient of the nth multipole term, and p_S and p_I have been written as vectors over the distinct angular variation orders. From (2.33) it can be seen that for the rigid cylinder, each multipole incident term only scatters into a multipole of the same order so that α_n relates the radiating nth order scattered field to the nth order incident field. In this regime the form of α is a diagonal matrix with entries α_n. As both the Hankel and Bessel spatial dependencies have zero phase at the origin, α_n describes the relative phase and amplitude of the nth order scattering coefficient, with reference to the incident field.

2.3 The Multipole Scattering Coefficients of 2D Meta-atoms

In chapter 5 the monopole and dipole scattering coefficients of meta-atoms are determined by fitting their incident and scattered fields to multipole expansions. In the previous section the scattered field of a rigid cylinder exposed to a plane wave was found to naturally lend itself to this form of expansion in solving the Helmholtz equation in polar coordinates. This section will present a brief mathematical argument as to the validity of a multipole expansion representing an arbitrary 2D field, such that the multipole scattering coefficients of an arbitrary 2D object (such as a meta-atom), which has been exposed to an arbitrary incident field can be defined in a similar way as they were for the cylinder.

In general, any 2D function $f(x, y)$ can be written in terms of its Fourier transform $F(k_x, k_y)$ via

$$f(x, y) = \frac{1}{(2\pi)^2} \int_{-\infty}^{\infty} \int_{-\infty}^{\infty} F(k_x, k_y) e^{i\vec{k}\cdot\vec{r}} dk_x dk_y. \tag{2.35}$$

Defining a polar coordinate transformation

$$\vec{k} = k(\cos\theta_k, \sin\theta_k), \quad \vec{r} = r(\cos\theta, \sin\theta), \tag{2.36}$$

where θ_k is the angle of $\vec{k}$ from the $\theta = 0$ axis, the inverse Fourier transform in polar

coordinates becomes

$$f(r,\theta) = \frac{1}{(2\pi)^2}\int_0^{\infty}\int_0^{2\pi} F(k,\theta_k)e^{ikr\cos(\theta-\theta_k)}kdkd\theta_k, \tag{2.37}$$

where similar working has been used as in (2.18). As $F(k,\theta_k)$ is periodic in θ_k it can be represented as the Fourier series

$$F(k,\theta_k) = \sum_{n=-\infty}^{\infty} F_n(k)e^{in\theta_k} \tag{2.38}$$

where $F_n(k)$ gives the spatial frequency dependence of each angular term. Putting this into (2.37) gives

$$f(r,\theta) = \frac{1}{(2\pi)^2}\sum_{n=-\infty}^{\infty}\int_0^{\infty}\int_0^{2\pi} F_n(k)e^{in\theta_k}e^{ikr\cos(\theta-\theta_k)}kdkd\theta_k \tag{2.39}$$

Now setting $\varphi = \theta - \theta_k$ we get

$$f(r,\theta) = \frac{1}{(2\pi)^2}\sum_{n=-\infty}^{\infty} e^{in\theta}\int_0^{\infty}\int_0^{2\pi} F_n(k)e^{-in\varphi}e^{ikr\cos\varphi}kdkd\varphi. \tag{2.40}$$

Using the same working as (2.21),

$$\frac{1}{2\pi}\int_0^{2\pi} e^{-in\varphi}e^{ikr\cos\varphi}d\varphi = i^nJ_n(kr) \tag{2.41}$$

so that

$$f(r,\theta) = \frac{1}{2\pi}\sum_{n=-\infty}^{\infty} i^ne^{in\theta}\int_0^{\infty} F_n(k)J_n(kr)kdk. \tag{2.42}$$

As the above Equation is an inverse Fourier transform of $f(r,\theta)$, it is inherently based on the orthogonality of the complex exponential and Bessel functions [10]:

$$\begin{aligned}\int_0^{\infty} J_n(k_1r)J_n(k_2r)rdr &= \frac{\delta(k_1-k_2)}{k_1}\\ \int_0^{2\pi} e^{inx}e^{-imx}dx &= 2\pi\delta(n-m).\end{aligned} \tag{2.43}$$

So that an equivalent definition of the inverse transform is just

$$f(r,\theta) = \sum_{n=-\infty}^{\infty} i^ne^{in\theta}\int_0^{\infty} F_n(k)J_n(kr)dk. \tag{2.44}$$

where the factor of $k/2\pi$ which appears due to orthogonality relations (2.43) can

just be placed in front of the forward Fourier transform. Now recognising that the function $f(r,\theta)$ is periodic in θ it can be seen that the inverse Fourier transform is essentially a multipole expansion in θ with coefficients $i^n \int_0^\infty F_n(k)J_n(kr)dk$:

$$f(r,\theta) = \sum_{n=-\infty}^{\infty} \left(i^n \int_0^\infty F_n(k)J_n(kr)dk \right) e^{in\theta}. \tag{2.45}$$

The above the result is completely general and shows that any function defined on the whole space can be represented as a multipole expansion, where similar results may be obtained in three dimensions, and for bounded functions [10]. In the case of an acoustic field of a single frequency satisfying the Helmoholtz equation (which is the type of filed exclusively of interest to this thesis) the integral over spatial frequency in (2.45) is only non-zero at the spatial frequency of interest k_0, and we have for the acoustic field $f(r,\theta)_{k_0}$:

$$\begin{aligned} f(r,\theta)_{k_0} &= \sum_{n=-\infty}^{\infty} i^n F_n J_n(k_0 r) e^{in\theta} \\ &= \sum_{n=-\infty}^{\infty} \beta_n J_n(k_0 r) e^{in\theta} \end{aligned} \tag{2.46}$$

where $F_n(k)$ is no longer a function of k and is instead denoted F_n, and the $i^n F_n$ terms have been multiplied together into β_n for convenience. Theoretically the expansion coefficients can now immediately be determined via the orthogonality relations in (2.43):

$$\beta_n = \frac{k_0}{2\pi} \int_0^{2\pi} \int_0^\infty f(r,\theta)_{k_0} J_n(k_0 r) e^{in\theta} r dr d\theta. \tag{2.47}$$

However, as will be discussed further in chapter 4 it is difficult in practise to perform this integration on experimental data.

The multipole series (2.46) should converge for an arbitrary acoustic field, although in the case of a scattered field the form of (2.46) is non-physical. This is due to fact that the field scattered of an object placed at the origin should obey the radiation condition for large radius, and the asymptotic behaviour of the Bessel function has both outgoing and incoming wave components [20]. To fix this, $J_n(k_0 r)$ can be replaced with the Hankel function of the first kind $H_n(k_0 r)$, which has the correct asymptotic behaviour in r. This is valid for a general 2D function representing a scattered field, as both $H_n(kr)$ and $J_n(kr)$ solve the radial part of the Helmholtz equation, and by Sturm–Liouville theory $H_n(kr)$ is also orthogonal over the whole

domain. So in the case of a scattered field we get

$$f(r,\theta)_{k_0} = \sum_{n=-\infty}^{\infty} \gamma_n H_n(k_0 r) e^{in\theta}, \tag{2.48}$$

with multipole terms γ_n. The explicit multipole expansions of general incident and scattered 2D fields can now be defined as

$$\begin{aligned} \text{Incident field } &= p_I = \sum_{n=-\infty}^{\infty} \beta_n J_n(k_0 r) e^{in(\theta-\theta_0)} \\ \text{Scattered field } &= p_S = \sum_{n=-\infty}^{\infty} \gamma_n H_n(k_0 r) e^{in(\theta-\theta_0)}, \end{aligned} \tag{2.49}$$

Where θ_0 is the angle of the incident field with respect to the x-axis (as defined in Fig. 2.1) and the coordinate transform $\theta \to \theta - \theta_0$ has been introduced so that these fields are defined with reference to the incident field. As before, ignoring the spatial dependency of the fields and writing them as vectors in the space of angular variations we have

$$\vec{p_S} = \alpha \cdot \vec{p_I}. \tag{2.50}$$

In the case of a rigid cylinder nth order incident terms only scatter into like terms so that α is a diagonal matrix. In the general case an object may scatter nth order terms into any other angular variation, such that the general form of α should be a full matrix of scattering coefficients with the cylinder being a special case where off-diagonal elements are zero. These off-diagonals couple the monopole and dipole response of the object, which in [22] was attributed to asymmetries in the scattering objects geometry. As this thesis only considers meta-atoms with high angular symmetry (see chapter 5), the assumption is made that these off-diagonals are also zero or small enough to be ignored so that multipole scattering coefficients can be defined similarly to (2.34):

$$\alpha_n = \gamma_n / \beta_n. \tag{2.51}$$

2.4 Summary

The acoustic wave equation was derived and the form of the monopole (α_0) and dipole (α_1) scattering coefficients of both a 2D rigid circular cylinder and general 2D geometry were defined. In the general case it was assumed multipole angular orders only scatter into like orders such that α_n can be determined directly from

the multipole expansion of the incident and scattered fields. This will be used extensively in chapters 4 and 5 when applied to meta-atoms.

Chapter 3

Experimental Apparatus and Methods

This chapter describes the acoustic measurement apparatus used in all experimentation contributing to this thesis. It details the modification and characterisation process of the apparatus, that was undertaken to ensure it is able to obtain accurate acoustic data. The experimental method developed to record the acoustic data is also defined.

3.1 Overview and Function of the Acoustic Field Measurement Apparatus

The main components of the apparatus used during experimentation consist of a sample test chamber constructed from a perspex parallel plate waveguide insulated along its edges with anechoic foam, a small loudspeaker placed inside of the waveguide which creates the acoustic field the samples are exposed to, and a low profile microphone mounted on an x/y axis gantry arm that records the 2D field. Labelled photographs and a diagram of the acoustic measurement system are given in Figs. 3.1 - 3.2, with relevant dimensions of the system also included. The waveguide structure and the mechanical and electrical components controlling the loudspeaker and microphone were assembled by a previous student, and are described in detail in [25].

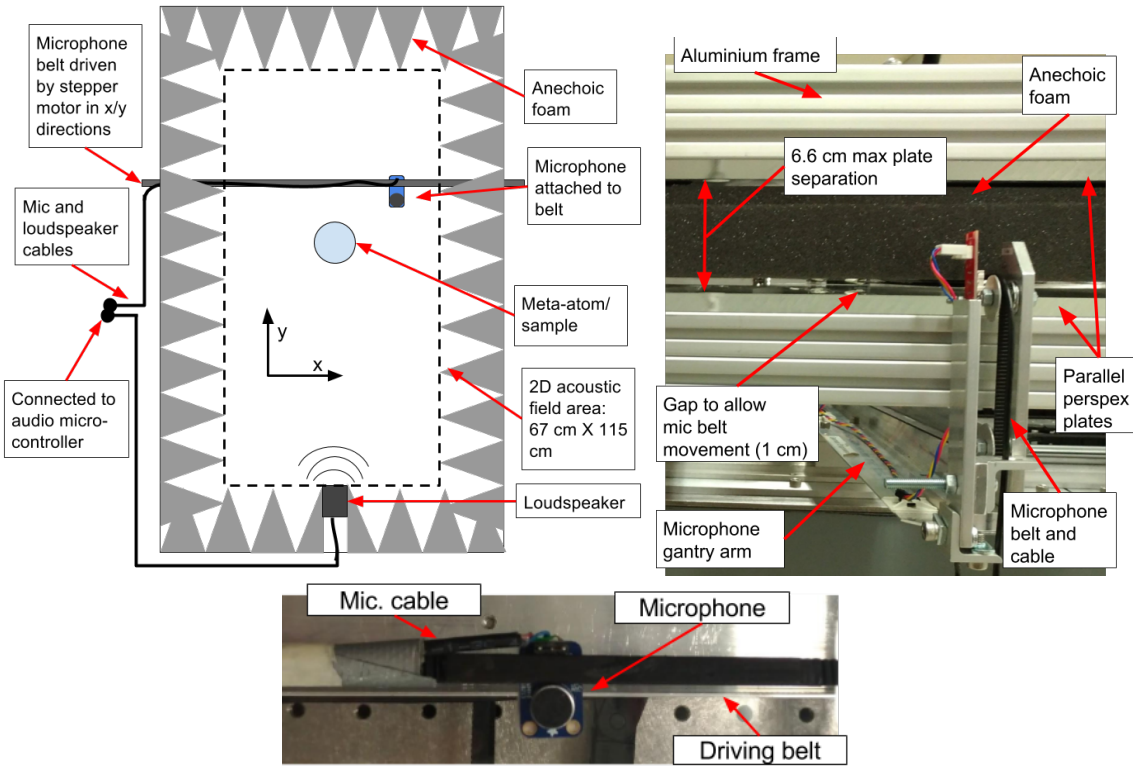

Figure 3.1: Top left: Diagram of acoustic measurement apparatus, showing the layout of components from above the parallel plate waveguide. The coordinate system convention used is in data analysis is also indicated. Top right: Side on and close up photograph of the waveguide with plates closed. The function of the microphone arm is indicated, showing the necessary gap to allow movement. Bottom: Close up of microphone sitting on top of perspex waveguide plate, it is glued to the driving belt.

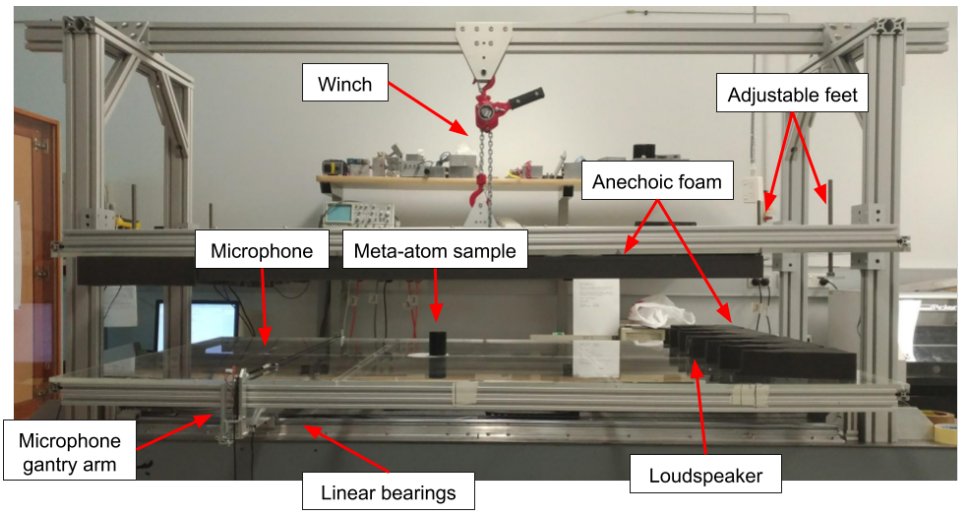

Figure 3.2: Side on view of the entire acoustic field measurement apparatus with the top plate lifted to allow access to the test chamber. The main functional components are labelled.

Both the input to the loudspeaker and the output signal from the microphone (Ada-

fruit electret with MAX9814 amplifier) are processed by a microcontroller (Teensy 3.2 with an audio shield) which in turn is connected to a computer via USB. Movement of the microphone is actuated by two stepper motors (NEMA17), which are controlled by a separate microcontroller (Arduino Mega 2560 with RAMPS v1.4 shield and A4988 stepper motor drivers), also connected to the computer. These stepper motors move the microphone using drive belts in the x and y directions as defined in Fig. 3.1. The microphone is attached to a belt (see bottom of Fig. 3.1) which actuates in the x direction, and the gantry arm the microphone belt is supported by, moves along the linear bearings to actuate in the y direction. This gives the microphone full movement in the xy plane. To allow this movement a small 1 cm gap is needed underneath the anechoic foam boundary (See Fig. 3.1). The microcontrollers are programmed in C++ to perform basic data recording or movement functions only, with more elaborate control structures being implemented through the computer using a Python environment as the interface. To record the acoustic field in the waveguide, the in phase and quadrature components (IQ) of the 2D acoustic field with reference to the loudspeaker source are sampled by scanning the microphone along a 2D grid path defined by a Python routine. IQ components are obtained using a cross-spectrum analysis algorithm implemented by the microcontroller that handles both the input and output audio signals. Here the reference signal is the internal digital output to the microphone. Further acoustic field data analysis is also performed in Python. Access to the inside of the waveguide is gained by lifting the top plate using the winch shown in Fig. 3.2, and the distance between the parallel plates can be set by using the adjustable feet.

3.2 Characterisation and Modification of Measurement System

3.2.1 Mechanical control over microphone

In order to accurately collect two-dimensional acoustic field data, complete control over the microphone position is required. During system testing, two primary issues effecting mechanical control over the microphone were identified. These were shudder in the microphone belt and arm whilst travelling in the y direction of the waveguide, and insufficient torque in the stepper motors while moving the microphone in the x direction. Both of these problems result in the driving stepper motor skipping steps; wherein the actual distance it has moved the microphone is less than what it was programmed to move. The effect on the acoustic data is that the re-

corded field becomes distorted due to inaccurate positional information at each at point. An example of this is shown in Fig. 3.3.

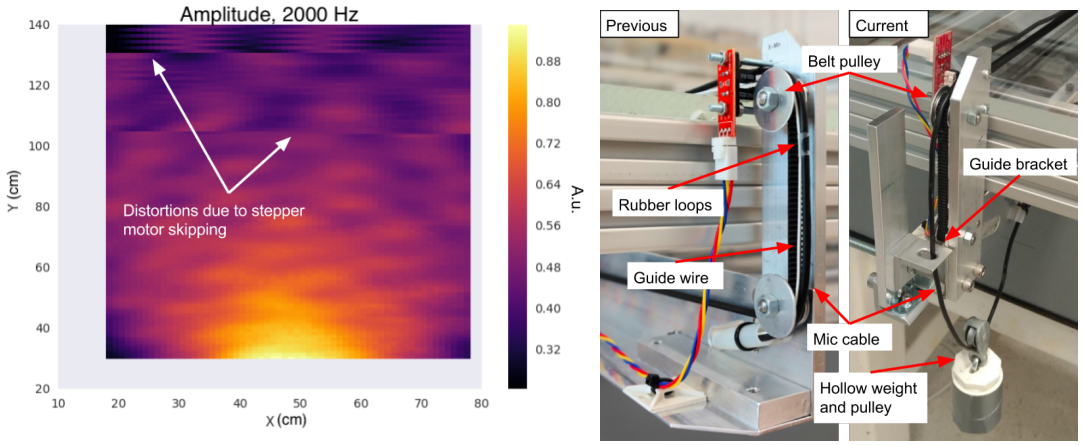

Figure 3.3: Left: Amplitude of acoustic field where the effects of the stepper motor skipping are apparent. Right: Comparison of previous cable guide system and the current one installed as part of the solution to the stepper motor skipping problem.

Further investigation of the shudder effect along the 'y' direction found that it was caused by irregularities in the linear bearings that the microphone arm moves along. The irregularities were found to have a resonant character, such that at certain travel speeds large undamped vibrations in the microphone arm and noticeable shudder were observed. The solution to this was to first increase the acceleration and deceleration rate of the y-axis stepper motor to their maximum value so that resonant speeds are skipped over quickly, and secondly to select a stepper motor speed through trial and error that avoided shudder. In the final measurement system set-up, the microcontroller connected to the stepper motors was programmed to allow a speed of 87 steps/s along the y-axis and 300 steps/s along the x-axis.

Insufficient torque in the x-axis stepper motor was found to be due to incorrect python code at the computer to microcontroller interface level, and a faulty microphone cable management system. The cable management system initially installed on the microphone arm consisted of a guide wire parallel to the microphone belt, with rubber loops attaching the cable to the wire. A cable tray underneath the arm would collect slack, and the microphone cable would be pulled with the belt, kept close to the belt by the guide wire (See Fig. 3.3). The problem with this system is that as the rubber loops pass over the belt pulley, they prevent the cable from bending causing it to stick at that point. A new cable management system was installed to overcome this issue. This consisted of a simple pulley attached to a hollow weight, so that the cable is fed through the weight's pulley, a guide bracket, and then onto the belt. The microphone cable is kept close to the belt by the tension caused by the weight, and it's hollow so that it's mass and subsequent tension

can be adjusted by adding or removing material. An image of this is given in Fig. 3.3. Although this system also applies a resistive torque to the stepper motor, the magnitude of the torque was reduced to an appropriate level by adjusting the mass in the weight. The error in the python code running on the computer was found to be a control structure in which the serial port object that microcontroller commands were written to was re-initialised for every command. This had the effect of turning the stepper motors on and off at every command, as the new serial port call initiates a stepper motor start up routine. When the motors are off they loose torque, and so should remain energised during use. The error was corrected for simply by altering the python code so that a single serial port object is made during a session. The benefits of these modifications can be seen in Fig. 3.6, where no distortion in the acoustic field is apparent.

3.2.2 Acoustic boundaries and parallel plate separation of waveguide

Acoustic reflections from the edges of the waveguide can significantly impact recorded field data. This is due to the fact that the analytical models results are compared with deal with the whole space, with radiation and/or boundary conditions applied for $r \to \infty$. It is therefore difficult to analytically account for them and remove their effect through post-processing. As such, the choice of acoustic boundaries in the waveguide that minimise reflections is essential. At the onset of testing the

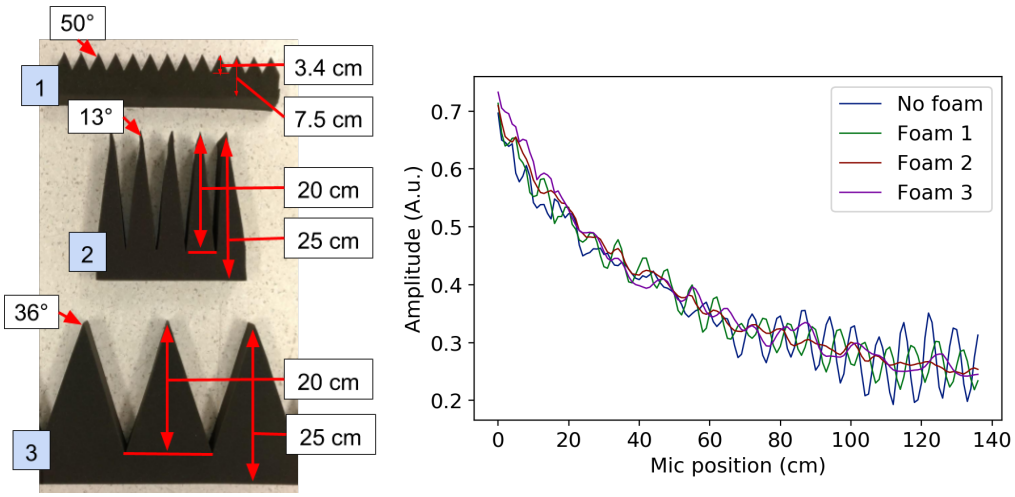

Figure 3.4: Left: Labelling and measurements of each anechoic foam tested to minimise relfections from waveguide edges. The number of each foam is highlighted blue. Right: Reflection test results of each foam, with 0 cm being near the loudspeaker and ∼140 cm being as close to the acoustic boundary as possible. The amplitude is recorded in arbitrary units (a.u.), and the test acoustic frequency used was 2500 Hz.

measurement system, two types of open cell acoustic foam were available to evaluate as waveguide boundary material. Both were of the general anechoic wedge shape designed to minimise reflections highlighted in the previous work section. These are labelled foam 1 and 2 in Fig. 3.4. Foam 1 was an off the shelf commercial product, and foam 2 was custom designed and cut by a previous student to have a geometry which better matched the general theory of acoustic anechoic wedges. In order to characterise the reflections from the foams a test was procedure was developed. The microphone was placed in the middle of the waveguide along the x-axis and the amplitude of the field recorded as a function of distance from the loudspeaker along the y-axis. The edging furthest from the speaker was altered from having no foam through to each foam tested while all other components of the waveguide were kept constant. The results of the testing are given in Fig. 3.4, and these clearly show the large decease in interference due to reflections that foam 2 provides. This is in accordance with the literature as the shape of foam 2 closely matches the optimal linear harvard wedge design given in [3], with a wedge length being roughly 80% of total thickness and a wedge tip angle of 13°, whereas foam 1 has an overly large wedge tip at 50°and small wedge length of 43% total thickness. A significant disadvantage of the foam 1 design is that its small wedges are difficult to pattern and custom cut. Due to this, and the fact that the numerical optimisation study in [12] found that broader wedge tips at 36°outperformed the narrower, an additional sample of the design labelled as foam 3 in Fig. 3.4 was created and tested in the same manner as previous foams. This design kept the foam 2 thickness of 25 cm, but broadened the wedge tips to 36°. As can be seen from Fig. 3.4, the broader tip design performs approximately equally as well as foam 2. Such that, as foam 3 was easier to produce and equally as effective it was selected to cover the remaining three boundary edges leaving foam 2 along the edge furthest from the speaker.

Another consideration in minimising the effects of boundary reflections is the gap beneath the anechoic foam to allow microphone movement. During system testing it was determined that the top plate had bowed upwards under it's own weight at the point of the winch connection. At the apex of the bowing the plates were measured to be 6.6 cm apart. Including this effect, the cutoff frequency of the waveguide is calculated using the same method given in the previous work section to be $f_c = c/2d = (343\ \text{ms}^{-1})/(2 \times 0.066\ \text{m}) \approx 2598$ Hz. Although the top plate could be lowered to increase the usable frequency range, there is a practical limit as to how small the plate separation may be due to the function of the acoustic anechoic foam edging. As shown in Fig. 3.1 the belt the microphone is mounted to requires a 1 cm gap underneath the foam to allow it move freely. When decreasing the plate separation the ratio of the gap to plate separation increases, which reduces

the efficacy of the anechoic foam allowing for more reflections from the edges. A practical trade-off at 6.6 cm was found, setting the gap under the foam to be ∼16% of total plate separation. To accommodate this gap the anechoic foam along the y direction is mounted to the top plate using double sided tape.

3.2.3 Function and placement of loudspeaker

During testing of meta-atoms or cylindrical samples, the acoustic field from the loudspeaker is used to approximate a plane wave incident on the sample. In order to meet this approximation, the phase front of the field must be as flat as possible and the amplitude have minimal variation. Theoretically this can be achieved by a single speaker acting as a point source, with the sample placed a number of wavelengths away where the phase front is flatter. During measurement system modification and testing, a number of different loudspeaker types and arrangements were trialled until a satisfactory incident field was produced.

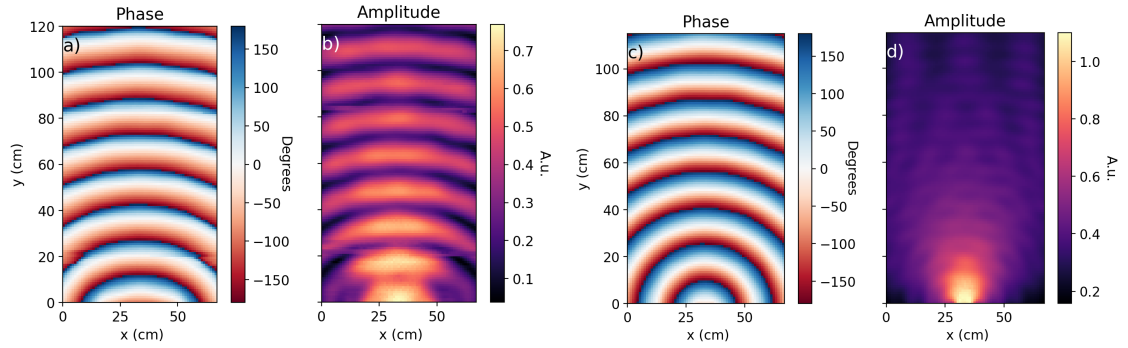

Figure 3.5: a) Phase of acoustic field in waveguide using an external 9 cm diameter loudspeaker source. b) The amplitude of the same field measured in arbitrary units (a.u.). c) Phase of the acoustic filed using an internal 5 cm diameter loudspeaker. d) Amplitude of internal loudspeaker field. The acoustic frequency in all plots is 2250 Hz.

The first loudspeaker arrangement tested consisted of 9 cm diameter loudspeaker placed at the external edge of the waveguide so that the field radiates into the test chamber. The acoustic foam boundary inside the waveguide was cut into a V shape with the speaker placed at its apex so that the field could propagate into the chamber with minimal reflections or diffraction effects due to the edging. This type of arrangement with an external speaker radiating into the chamber was described in the previous work section, and was successfully used in [15]. The recorded amplitude and phase inside the waveguide using this set up is given in Fig. 3.5. The phase of the recorded field closely resembles that of a point source, however the amplitude shows a distinct standing wave interference pattern. This interference was found to be

caused by the comparatively large reflective surface that the loudspeaker diaphragm presents over the frequency range of interest. After trialling different anechoic foam and loudspeaker configurations, it was determined that to remove the interference a much smaller 5 cm diameter speaker should be installed and placed inside of the waveguide. This was positioned flush with the anechoic foam wedge tips, shown in Fig. 3.1. As can be seen from the phase and amplitude plots in Fig. 3.5, the smaller speaker behaves much more like an ideal point source, and so was used for further experimentation.

3.2.4 Characterisation of finalised acoustic measurement apparatus

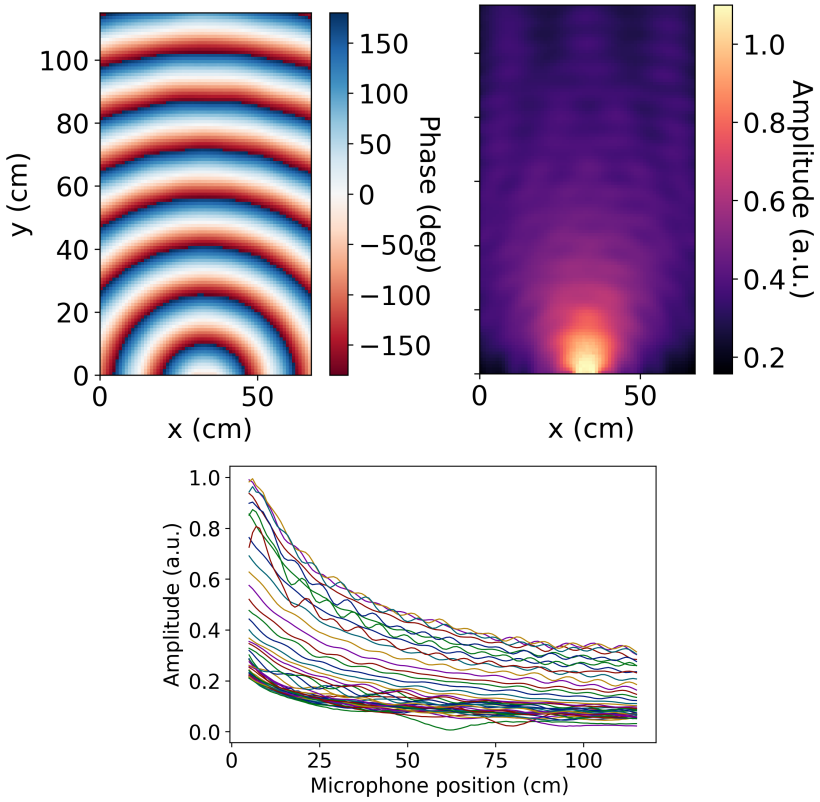

Figure 3.6: Top: Phase and amplitude of acoustic field in finalised measurement system at 2250 Hz. Bottom: Amplitude of acoustic field as a function of distance away from microphone (0 cm being closest), plotted for frequencies in the range 500 - 2500 Hz in 100 Hz increments. Amplitudes shown in arbitrary units (a.u.).

The acoustic measurement system was characterised once all modifications were completed, the results of which are given in Fig. 3.6. Here it can be seen that in the waveguide the phase of 5 cm diameter loudspeaker closely approximates that of a point source, and from the amplitude plots as a function of distance; that reflections

from the edges are minimal and smaller than in Fig. 3.4. Also all distortions in the recorded 2D field are now removed. However from the 2D plot of the amplitude, there are still reflections present in the waveguide, although these are assumed to be at acceptable levels.

3.3 Method of Obtaining Acoustic Field Data

The method used to record the 2D acoustic field data of meta-atom samples can be summarised as follows. The sample was placed in the centre of of the x-axis of the waveguide 67 cm away from the speaker along the y-axis where the phase front is relatively flat. The height of the sample was kept at 66 mm, so that the both the top and bottom surfaces would sit relatively flush with the waveguide plates. A Python routine was then ran which records the total field in it's complex IQ components over a range of frequencies. This was done by scanning the microphone along the x and y directions, and recording the field at 1 cm increment points along the path over the frequency range of interest. The sample was then removed and the complex incident field recorded at the same points and frequencies as before. The scattered field can then be obtained by subtracting the incident field from the total field.

To simplify later data analysis, the recorded scattered and incident fields should have an origin which is aligned with the geometric centre of the sample. To achieve this, a mark was made on the vertical side of the sample that coincides with an axis passing through it's geometric centre. At the start of the acoustic scan the microphone was positioned as close as possible to the sample, in line with the mark and hence the samples geometric centre. Given this initial condition and the known diameter of the meta-atom sample a Python function was written that correctly defines the position of the microphone with reference to the samples centre, and scans the 2D field.

As the microphone is attached to a stepper motor belt spanning the waveguide, the total field has to be recorded in two parts with one on either side of the meta-atom. To do this the scan was paused once the first side was completed, the sample was removed while the microphone was repositioned to the other side, and then the sample was replaced and the scan continued. The microphone movement was always performed programmatically to maintain accurate position information.

An important factor in ensuring the accuracy of the field data was to allow enough time for the system to come to rest before recording the acoustic field at that point. Specifically the time between a microphone movement instruction and data capture,

and the time between individual frequency data capture was critical. After a movement instruction, the microphones position would be unstable for approximately 1.5 s, so that a puase of this length was included in the Pyhon code. This instability was due to a combination of friction with the surface of the waveguide and relatively large oscillations of the cable weight, which would damp out quickly. Smaller oscillations of the cable weight taking longer to damp out were not able to move the microphone and did not generate any measurable acoustic interference. It was also found that in order to avoid frequency overlap caused by lag in the input/output response of the measurement system, a pause of at least 0.3 s was necessary between successive frequency inputs to the loudspeaker.

To avoid noise in the lab or other sources of acoustic interference detracting from results, multiple measurements at each microphone position were recorded and the average taken. However, the number of repetitions was kept relatively low at 2 to 3 as a scan could take 15-20 hrs to complete for a typical frequency range of interest, and increasing the time to complete a scan further was not feasible. To improve the accuracy without increasing scan time, the validity of the data was checked at each point using a number of condition statements included in the Python code. The first of these was to check that the maximum variance in the repetitions was less than a threshold value in order to account for any significant noise lasting a short period of time occurring at that microphone position. The second was that the difference in maximum amplitude of neighbouring points should also be less than a threshold value to account for sources of noise which may last a longer period of time and be constant over all repetitions at a point. If any of these checks failed, the system would pause for a period of time and then attempt to retake the data point. If a number of these attempts failed it would wait until further input from a person to check on the scan and allow it to continue.

During all scans the maximum frequency used was 2500 Hz, below that of the cut-off frequency of 2598 Hz, so that it could be ensured a 2D propagating field with no higher order modes existed in the waveguide.

3.4 Summary

The steps taken to modify and characterise the acoustic measurement apparatus were outlined. A characterisation of the finalised measurement system found that all distortions in the recorded acoustic field data had been removed, and that some reflections from the edges of the waveguide are still apparent, but have been minimised. The method used to record experimental acoustic field data was also described.

Chapter 4

Data Analysis

In the previous chapter the function of the acoustic measurement system was defined and the method used to collect experimental acoustic data described. This chapter will develop the data analysis method used to extract the monopole and dipole scattering coefficients from that data. The method will also be verified by comparing experimental determined scattering coefficients of a rigid cylinder, with the analytical expression from chapter 2.

4.1 Method of Extracting the Monopole and Dipole Scattering Coefficients from Experimental Data

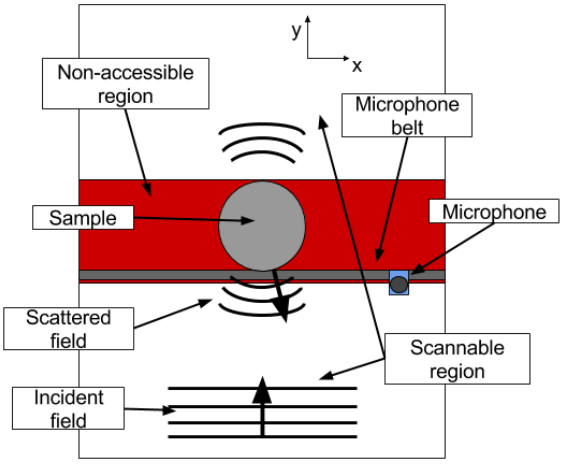

Figure 4.1: Diagram of the acoustic field measurement apparatus while performing a scan. The regions of the xy plane accessible to the microphone are labelled.

In order to extract the multipole scattering coefficients from recorded acoustic field data α_n, and specifically the monopole α_0 and dipole α_1 terms the multipole expansion coefficients β_n and γ_n of the incident and scattered must be determined.

The most theoretically robust way of doing this would be to integrate the acoustic field data as in (2.46), where the relationship $J_n(kr) = \frac{1}{2}\left(H_n^{(1)}(kr) + H_n^{(2)}(kr)\right)$ [20] could be used in the case of the scattered field to find the components corresponding to the radiating $H_n^{(1)}(kr)$ spatial dependency. This method would ensure that only the angular variation of interest contributes to the coefficient being calculated. However, as mentioned in section 2.3 this cannot be performed on the acoustic data recorded. This is because in the measurement apparatus the entire 2D domain around the sample is not accessible by the microphone. As can be seen in Fig. 4.1, only the regions in front of and behind the sample shown in white can be scanned, whereas the microphone belt prevents the regions in red from being reached. In this subset of the 2D domain, the angular basis functions $e^{in\theta}$ are not orthogonal, such that the relationship in (2.46) no longer holds. To overcome this, a data fitting scheme was adopted instead of numerical integration. Recognising that from (2.49) the incident and scattered fields are linear in β_n and γ_n a complex linear least squares fitting procedure was performed using (2.46) with β_n and γ_n as the fit parameters. Once the expansion coefficients were determined via fitting, the scattering coefficients could then be found using (2.51). In comparison to integration, this method has a drawback in that it is possible for the effects of higher order angular terms to be fitted into the β_0/β_1 and γ_0/γ_1 coefficients, or that effects from these coefficients themselves are fitted into higher order terms. Although, as will be shown in the following sections this does not appear to significantly detract from results.

4.2 Complex Linear Least Squares Fitting and Error Analysis

The algorithm used to perform the complex linear least squares fitting was the *gelsy* routine from the LAPACK library [1], implemented using the Scipy package in Python. The residuals function that the was minimised by the algorithm was defined as

$$\chi^2 = |\vec{y} - X \cdot \vec{a}|^2 \tag{4.1}$$

where $|..|$ denotes the l^2-norm, $\vec{y}$ is the vector of all recorded acoustic field data points, $\vec{a}$ is the vector of containing the fit parameters and X is the matrix containing the spatial dependency of the multipole expansions, with the columns representing distinct angular variations. In the case of fitting an incident field the components $a_n = \beta_n$ and X is determined using $J_n(k_0 r)e^{in(\theta-\theta_0)}$ with distinct n along its columns. Although the acoustic field data recorded is the average of a few repetitions, the re-

siduals function does not contain any weights based on the variance of the data points in $\vec{y}$ to avoid skewing the fit process. Despite the fact a particular y_i might have a low variance, this does not capture the effects of reflections from the waveguide edges or other systematic errors in the measurement apparatus, and so the weights were left out. Under this regime, the covariance matrix of the fit parameters C is given by [26]:

$$\begin{aligned} C &= \frac{|\vec{y} - X \cdot \vec{a}_{min}|^2}{N_{free}} (X^\dagger \cdot X)^{-1} \\ &= \sigma_f^2 (X^\dagger \cdot X)^{-1}, \end{aligned} \tag{4.2}$$

where $\vec{a}_{min}$ are the parameters found that minimise χ^2, N_{free} is the degrees of freedom of the fit and $X^\dagger$ indicates the hermitian transpose of X. In the above, the variance of the overall fit σ_f^2 is used to estimate the error in the recorded data and scale the covariance terms appropriately. The standard deviation of the error in the fit parameters was then taken from the diagonals of the covariance:

$$\sigma_{a_n} = \sqrt{c_{nn}}. \tag{4.3}$$

During analysis the normalised residuals of a fit were also examined to gauge the relative error, where this can be defined as

$$\frac{|\vec{y} - X \cdot \vec{a}_{min}|^2}{|\vec{y}|^2}. \tag{4.4}$$

4.3 Verification of Extraction Method

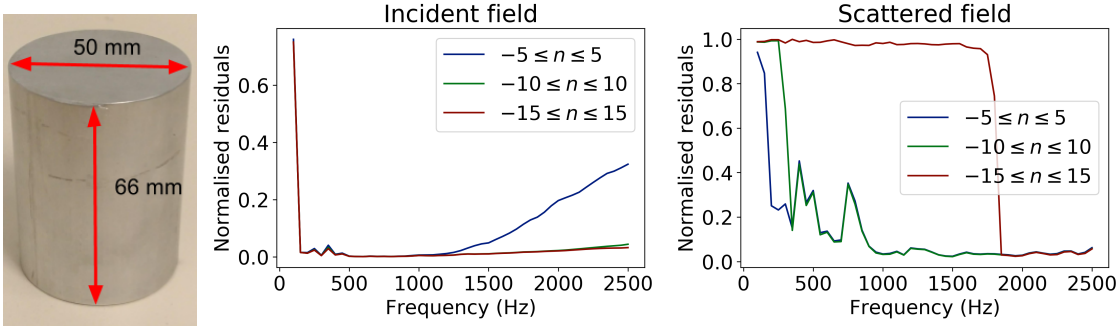

Figure 4.2: Left: Rigid cylinder scattering coefficients were extracted from. Right: Plots showing the normalised residuals of fitting the scattered and incident fields of the cylinder to (2.49) for various orders of n.

To verify that the least squares fitting method was able to accurately extract the monopole and dipole scattering coefficients, the coefficients of a rigid cylinder were

determined using the fitting method, and compared to the analytically derived values in (2.34). The experimental rigid cylinder was a 66 mm length of solid aluminium rod, with a 50 mm diameter shown in Fig. 4.2, and the results of extracting it's scattering coefficients are given in Fig. 4.3. During the analysis, the speed of sound used in calculations was 343 m/s, taken at 20℃ [11], and the largest angular variation fitted to the data was of 10th order. This number was reached using trial and error to try and minimise the normalised residuals over the frequency range of interest. As can be seen from Fig. 4.2, only using up to 5th order terms causes poor fitting in the incident field, whereas going beyond 10 up 15th order dramatically over-fits the scattered field. Using $-10 \leq n \leq 10$ provides normalised residuals less than about 5% above frequencies of 1000 Hz, so this was chosen to calculate the coefficients for the rigid cylinder and the meta-atoms considered in chapter 5. The generally large residuals below 1000 Hz seen for all angular orders is caused be the small 5 cm radius loudspeaker in the measurement apparatus being unable to accurately reproduce these low frequencies, and the fact that the anechoic foam boundaries absorb sound better at higher frequencies [3].

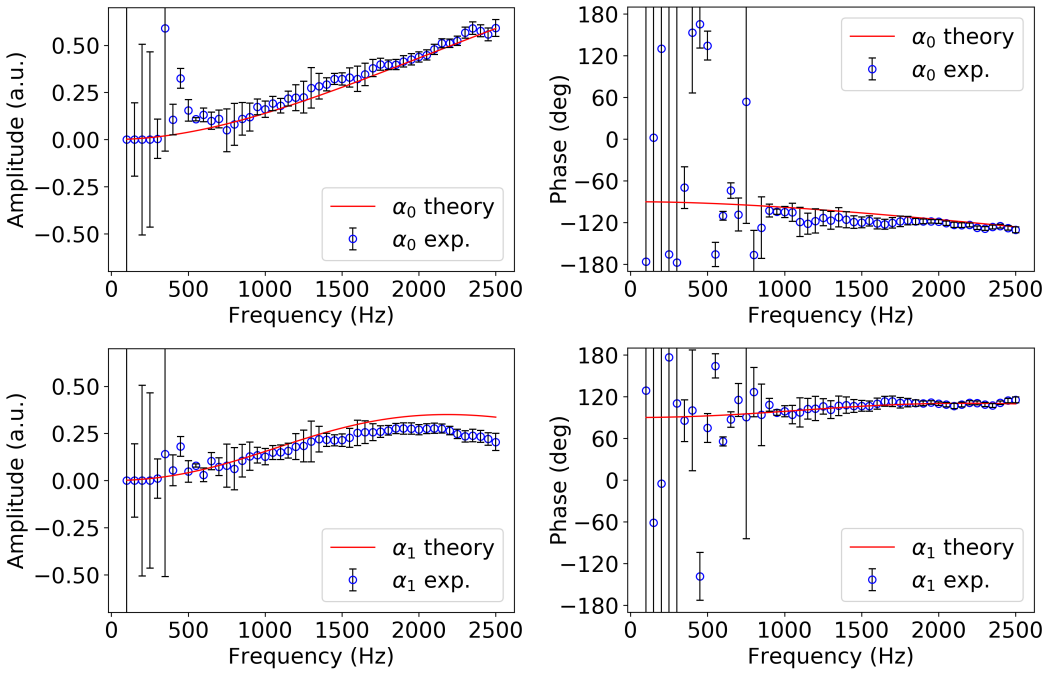

Figure 4.3: Results of extracting the monopole (α_0) and dipole (α_1) scattering coefficients of a 50 mm diameter rigid cylinder by fitting the experimental fields to (2.49) and comparing the results to (2.34). Error bars show $\pm 2\sigma$ in α_0 and α_1.

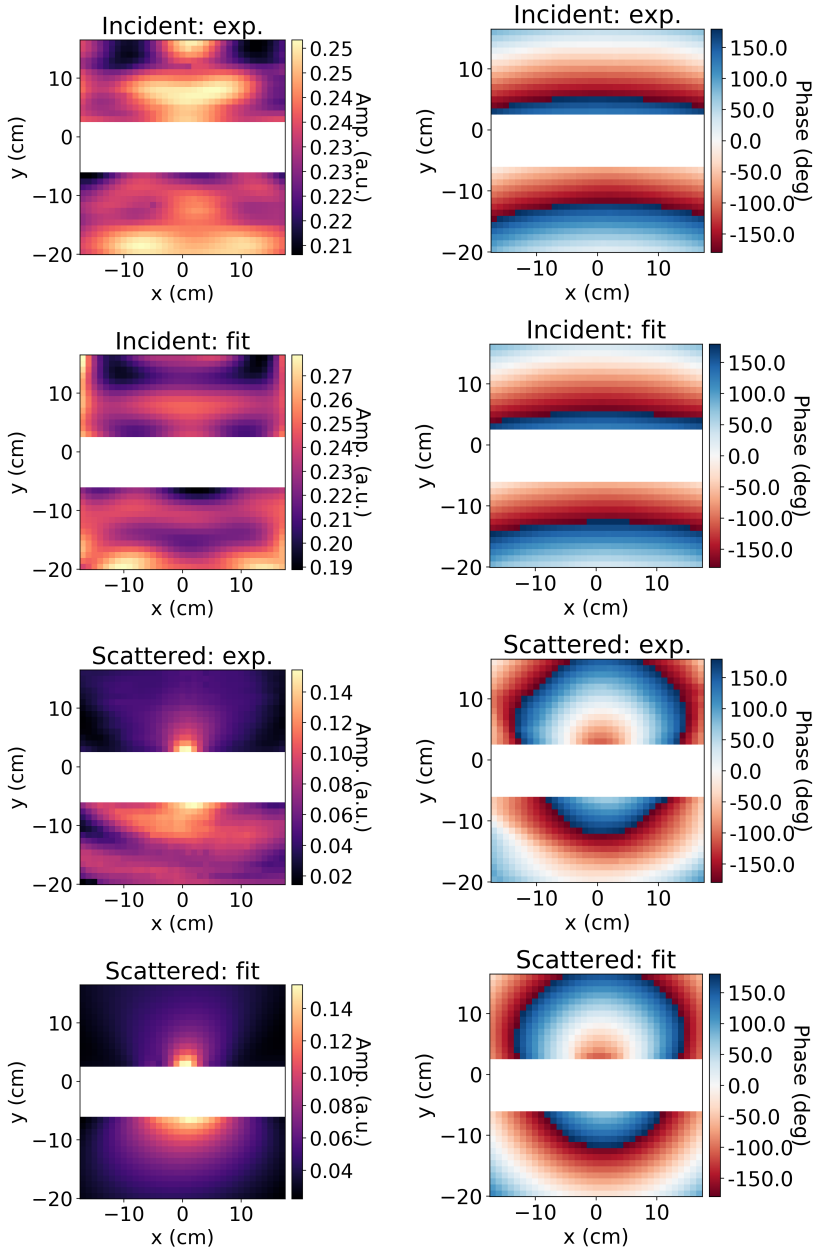

Figure 4.4: Examples of fitting the incident and scattered fields of a 50 mm diameter rigid cylinder to the multipole expansions in (2.49) to 10th order terms. The experimental and fitted fields are shown, as are the amplitude of the fields in arbitrary units and the phase in degrees. The acoustic field is incident from the bottom ($\theta_0 = \pi/2$) and the centre of the cylinder is situated at the origin. The acoustic frequency in all plots is 2000 Hz.

Examining the results of extracting the coefficients in Fig. 4.3, above 1000 Hz they generally agree reasonably well with the theoretical values of the scattering coefficients, with experimental values converging to the theoretical at higher frequencies. This is in keeping with the observation that the residuals decrease with increasing frequency, implying that systematic errors in the measurement apparatus are lessened at higher frequencies and the observed scattering is closer to the theoret-

ical. The main exception to this is that there is a trend for the dipole amplitude to be slightly lower than theoretical values, especially near 2000 Hz where it diverges away from the theoretical curve. The error in the phase and amplitude of α_0/α_1 was taken from error in the β_n/γ_n multipole expansion coefficients defined in (4.3) and then propagated using standard error propagation methods. In the plots the size of the errorbars is 2 standard deviations ($\pm 2\sigma$) of the error in α_0/α_1, as assuming normally distributed parameters, this represents the 95% confidence interval of the fit parameters, and shows that the theoretical coefficients generally do lie within the error margin of the experimental parameters, even at higher frequencies where the standard error becomes small.

In Fig. 4.4 examples of the experimental and fitted acoustic fields are provided. This shows some possible explanations for the slight discrepancies between theoretical and experimental coefficients in Fig. 4.3. The phases of the fitted fields closely match those of experimental, whereas the amplitude of the bottom part of experimental scattered field has some variations not captured by the fitting, most likely due to small reflections in the waveguide. This is in keeping with the observation that phase of the determined dipole coefficient has less discrepancy than it's amplitude, as well as the characterisation of the measurement apparatus in chapter 3.

4.4 Summary

A method of extracting the monopole and dipole scattering coefficients from the recorded 2D acoustic field data was developed. This uses a complex linear fitting algorithm to fit the recorded data to the multipole expansions of the incident and scattered fields described in chapter 2. The method was also verified by comparing experimental values of the scattering coefficients of a rigid cylinder with the analytical values. These were found to agree, especially at higher frequencies where there is less experimental error present in the measurement system.

Chapter 5

Design, Fabrication and Characterisation of Meta-atoms

Having developed a method of extracting the monopole and dipole scattering coefficients in the previous chapter, this chapter will apply this method to fabricated meta-atoms. Designs previously presented in the literature will be characterised and the results compared to simulated values also taken from the literature. Modified versions of one of these designs will also be examined, for the sake of interest.

5.1 Selected Meta-atom Designs and Fabrication Methods

In total four meta-atoms were fabricated and characterised for this thesis. Two of these had already been presented in [4] and [17] and the others consisted of slight modifications to the design in [4] in order to try and observe a shift in the monopole and dipole resonances. The designs in [4] and [17] were selected as they had been numerically modelled to determine expected multipole resonances and their symmetrical geometry was shown to not couple the monopole and dipole scattering in [4] which is an important assumption of the extraction method. Diagrams of the designs are shown in Fig. 5.1, and photos of the fabricated meta-atoms in Fig. 5.2. All of the designs were fabricated by 3D printing them using PLA plastic with a 0.1 mm layer thickness, to a height of 66 mm. The top of the meta-atom is left open to ease fabrication, and due to it sitting relatively flush with the top plate of the waveguide a printed top is not necessary. The working principle of these meta-atom designs is similar to that of the labyrinthine meta-surfaces described earlier. Here, the narrow sub-wavelength zig-zag channels increase the propagation length of a sound wave has to travel as it enters the exterior to the centre radius. Consequently it possess a high refractive index relative to the background medium [4], and the eight-fold angular symmetry allows for multipolar resonances to be sustained. Where

changing the met-atoms internal geometry allows for the frequency of the resonances to be controlled [4].

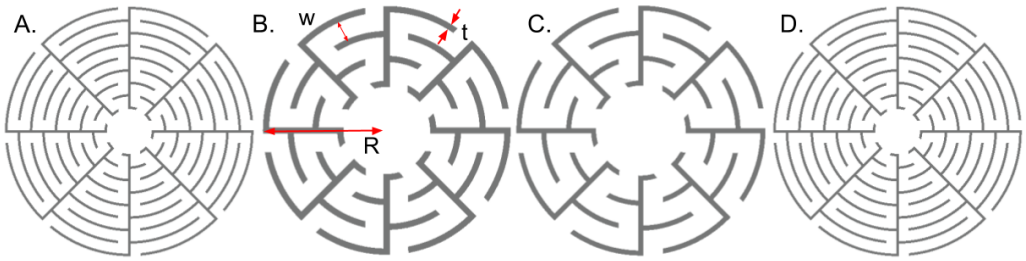

Figure 5.1: Diagrams of the meta-atom designs that were characterised. Meta-atom A was taken from [4], B from [17] and C and D modified versions of A. The diagram of meta-atom B defines the parameters wall thickness 't', channel width 'w' and meta-atom radius 'R'. For A: R = 50 mm, w = 4 mm and t = 1 mm B: R = 40 mm, w = 6 mm, t = 2 mm. C: R = 25 mm, w = 4 mm, t = 1 mm. D: R = 25 mm, w = 2 mm, t = 0.5 mm.

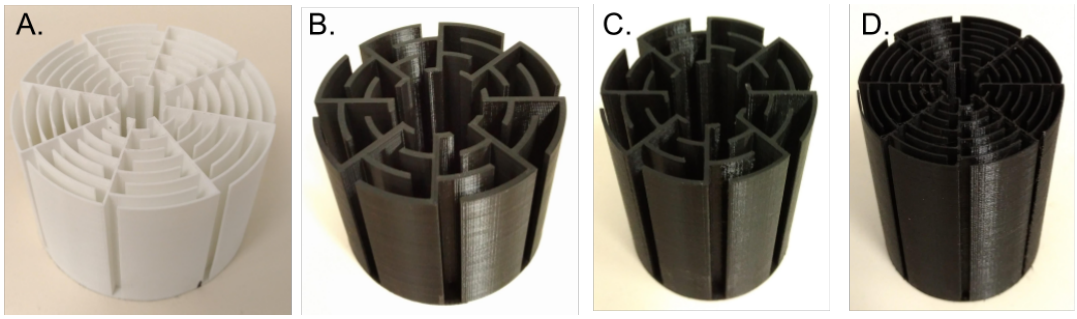

Figure 5.2: Fabricated meta-atoms, the diagrams of which are in Fig. 5.1. All meta-atoms were 3D printed using PLA plastic with a 0.1 mm layer thickness to a 66 mm height.

5.2 Determining the Acoustic Scattering Coefficients of Meta-atoms

5.2.1 Meta-atoms presented in the literature

Meta-atom A

In the paper featuring meta-atom A, Cheng et al. [4] perform a semi-analytical derivation of the multipole expansion coefficients of the scattered field (γ_n) with the aid of numerical simulations. They found that the meta-atom should have a monopole resonance at 518 Hz and a dipole resonance at 1080 Hz. The results of their calculations are given in Fig. 5.4, where they also include the calculated quadropole expansion coefficient. To compare with those results the dipole and monopole

scattering coefficients of meta-atom A were experimentally determined by fitting the scattered and incident fields to the multipole expansions in (2.49) as described in chapter 4, the results of which are in Fig. 5.3, as is the normalised residuals of the fitting. As in [4] they present the multipole expansion coefficients (γ_n) of the scattered field, and not the scattering coefficients which have been normalised with respect to the incident field (α_n) as defined here, the determined α_n need to be modified for a direct comparison. This can be done by approximating the incident field as a perfect plane wave, in which case from (2.34) $\gamma_n = i^n \alpha_n$. This conversion has also been included in Fig. 5.3 to facilitate a direct comparison, however it does not effect the monopole phase or either coefficients amplitude.

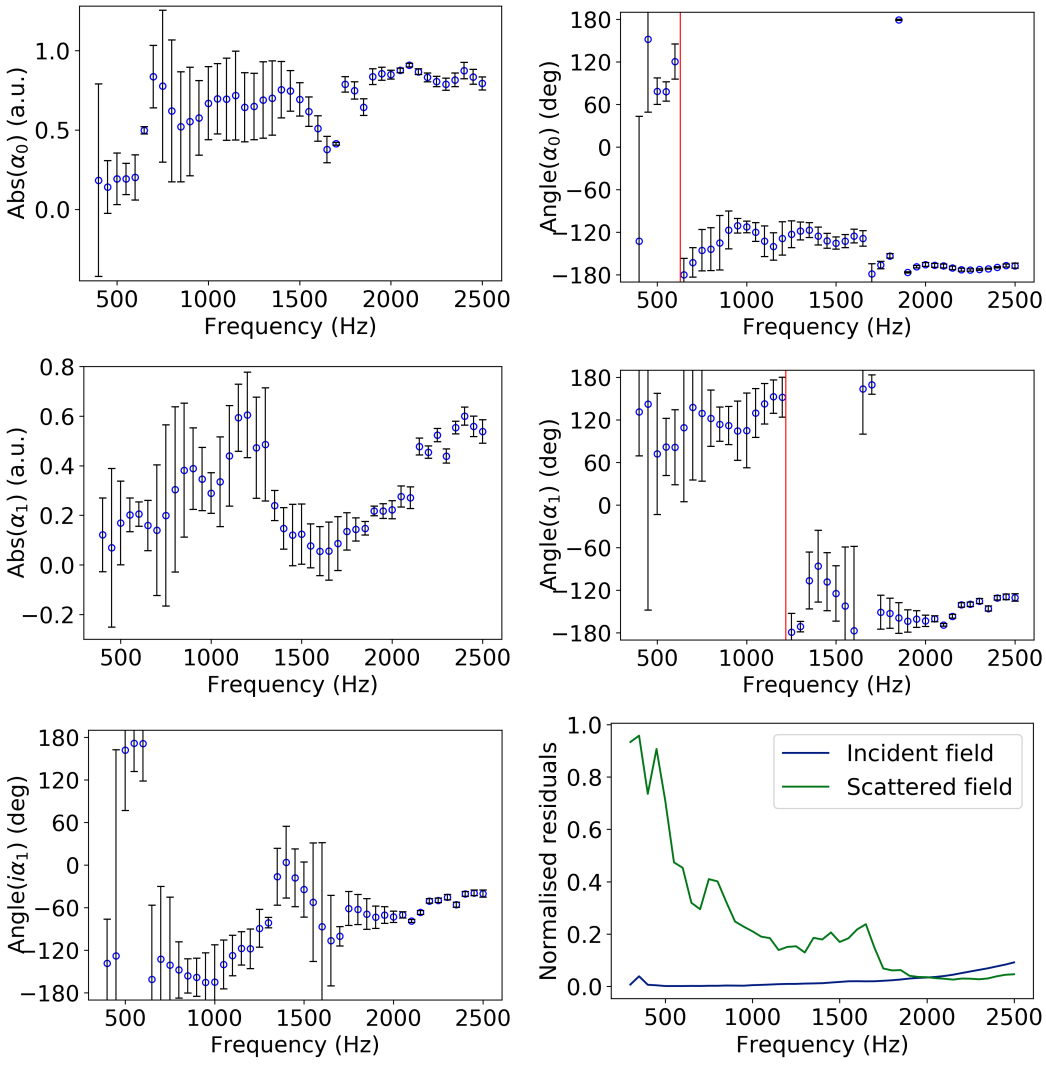

Figure 5.3: Top and middle: Results of extracting the scattering coefficients of meta-atom A. The zero crossings of the phase, associated with resonances have been indicated in red, for α_0 at 630 Hz, α_1 at 1220 Hz. Bottom left: Scattered field expansion coefficient $i\alpha_1$ for comparison with Fig. 5.4. Error bars correspond to a standard deviation in the error propagated from the fit parameters. Bottom right: Normalised residuals of fitting the scattered and incident fields.

Comparing Figs. 5.3 and 5.4, the experimentally observed resonance in the amplitude of the dipole coefficient is much broader than that derived in [4], which is most likely due to increased loss in the real meta-atom such as viscous drag with the surface that was not fully accounted for in [4]. As the resonance peak is broad, the experimental resonant frequency is instead defined where the scattered field is in phase with the incident field such that the phase of the scattering coefficient is zero. These zero crossings are easily seen in Fig. 5.3 and marked in red. Here the monopole resonance is found to be at 630 Hz, and the dipole at 1220 Hz which are 112 and 140 Hz respectively, above the calculated resonances. This shift is again likely due to effects not considered in [4], such as non-perfectly rigid walls transmitting some of the sound or other properties of the real meta-atom material.

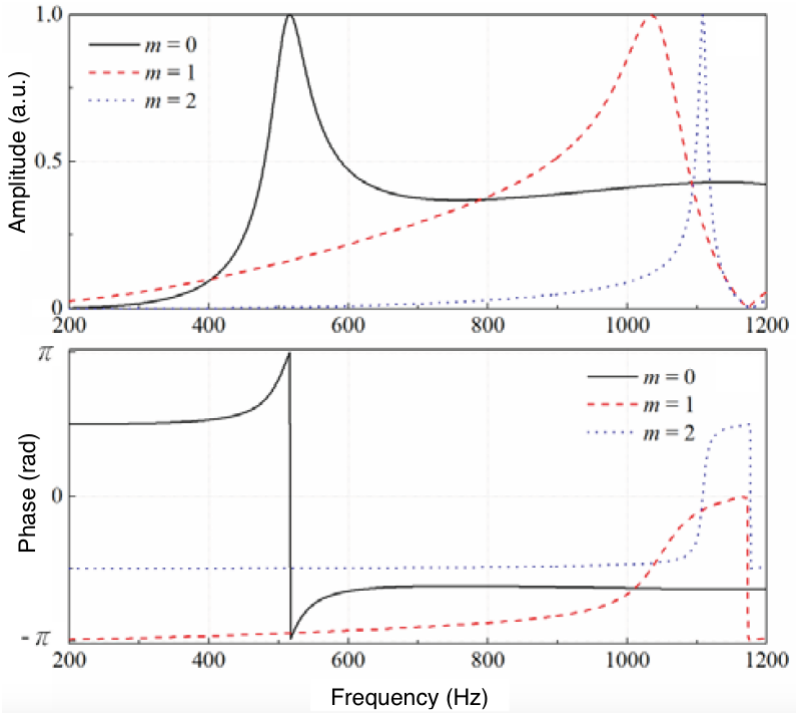

Figure 5.4: Semi-analytically derived scattered field expansion coefficients of meta-atom A, taken from [4]. Here m represents the angular order of the coefficient.

Looking at the phases in Fig. 5.4 compared to the phases of α_0 and $i\alpha_1$, the experimental values behave similarly. For α_0 in both plots there is a sharp increase to 180° before resonance, followed by a dip to -180° and a plateau at about -100°. $i\alpha_1$ is less similar with an anomalous peak to 180° near 500 Hz, however the rise from near -180° to 0° slightly after resonance can be seen in both. These findings are also effected due to the error in the experimental values in Fig. 5.3 being quite large, especially at low frequencies where the monopole resonance cannot be discerned in the amplitude plot. This is most likely due to to the size of the meta-atom relative to the acoustic scan area. The scan area was kept to an area below or equal to

40 cm X 40 cm when characterising meta-atoms to avoid reflections from the edges and reduce the length of time for a scan. The large meta-atom A radius at 50 mm reduces the percentage of the angular field captured around it, which would increase the error of the fitting.

Meta-atom B

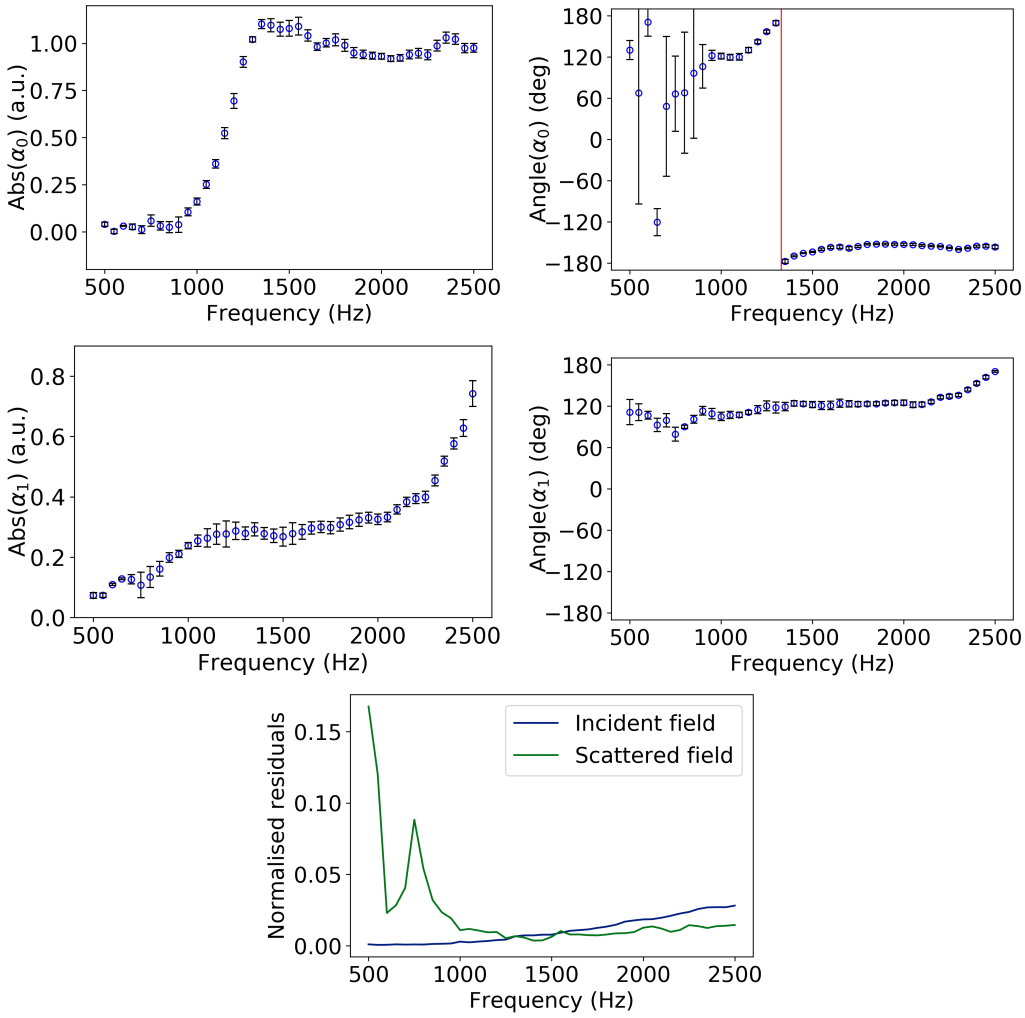

Figure 5.5: Top and middle: Results of extracting the scattering coefficients of meta-atom B. The zero crossing of the phase associated with the resonance has been indicated in red, for α_0 at 1330 Hz. Error bars correspond to a standard deviation in the error propagated from the fit parameters Bottom: Normalised residuals of fitting the scattered and incident fields.

In the experimentally determined scattering coefficients of meta-atom A the dipole resonance is reasonably distinct, however the monopole resonance near 500 Hz is more difficult to discern as this low frequency region is subject to the most error. In order to see a monopole resonance more clearly, Meta-atom B was selected, as

Lu et al. [17] derive using the same method as in [4] that Meta-atom B should have a monopole resonance at 1360 Hz which would place it in a less error prone frequency region. Lu et al. [17] do not calculate any other resonances apart from the monopole, so Meta-atom B was characterised only to compare this value. The results of determining its scattering coefficients are provided in Fig. 5.5. From this figure the experimentally determined monopole frequency is 1330 Hz, a result which is within the 50 Hz data point spacing from the expected 1360 Hz. This is much more accurate than the resonances seen in meta-atom A, and there is also a large reduction in the error of the scattering coefficients. This could be due to a number of reasons, one of which is the reduced 40 mm radius allowing for a larger angular percentage of it's field to be captured in an acoustic scan. Also, the thicker walls of meta-atom B (2 mm compared to 1 mm of meta-atom A) and the wider channels (6 mm compared to 4 mm) would reduce the effects of material properties such as transmission through a wall or viscous drag with the edges of the channels.

5.2.2 Modified meta-atom designs

Meta-atom C

Having experimentally observed reasonably distinct monopolar and dipolar resonances in the scattering coefficients of meta-atoms A and B, meta-atoms C and D were designed by modifying A to try and shift these resonance frequencies. As neither of these designs were modelled, the modifications were simply based on heuristic principles derived from the meta-atoms working principles in [4]. Meta-atom C was designed by keeping the internal channel structure of meta-atom A, but reducing it's external radius by half; to 25 mm. The assumption here being that having the same effective properties, but a halved radius should shift the monopole resonance from 630 Hz observed previously, to somewhere above 1200 Hz. The results of this are given in Fig. 5.6. Here there is a distinct resonance at 2170 Hz; higher than what was expected, which most likely indicates some non-linearities in the properties of this type of meta-atom. Due to the estimate nature of the expected resonance, this result to some extent confirms that decreasing the meta-atom radius while keeping other parameters constant will increase it's monopolar resonance. The error in the scattering coefficients here is also reduced when compared to the results of meta-atom A, which is in keeping with the trend that smaller met-atoms allow for improved fitting of the acoustic fields.

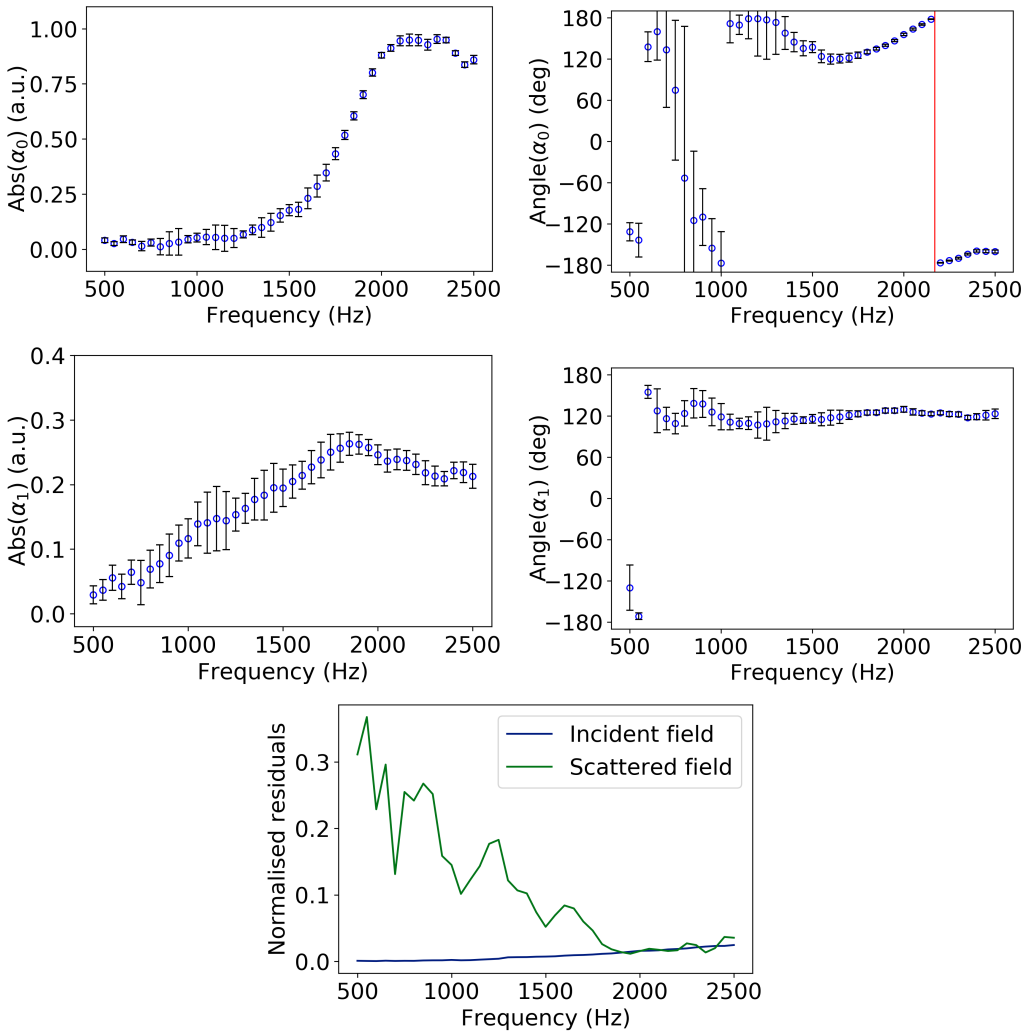

Figure 5.6: Top and middle: Results of extracting the scattering coefficients of meta-atom C. The zero crossing of the phase associated with resonance has been indicated in red, for α_0 at 2170 Hz. Error bars correspond to a standard deviation in the error propagated from the fit parameters Bottom: Normalised residuals of fitting the scattered and incident fields.

Meta-atom D

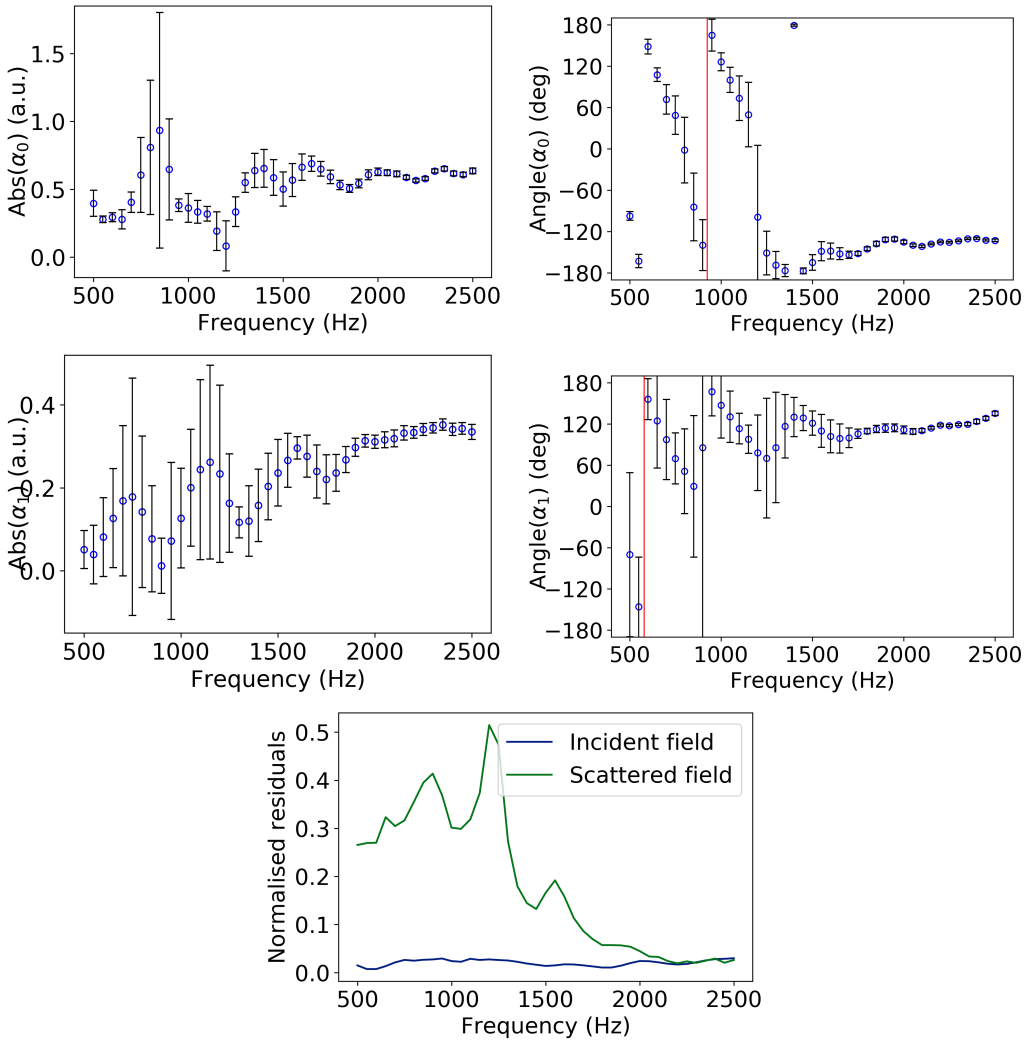

Figure 5.7: Top and middle: Results of extracting the scattering coefficients of meta-atom D. Some zero crossings of the phase can tentatively be observed to indicate resonance, these have been indicated in red, for α_0 at 925 Hz and α_1 at 580 Hz. Error bars correspond to a standard deviation in the error propagated from the fit parameters Bottom: Normalised residuals of fitting the scattered and incident fields.

Meta-atom D was design by scaling all the dimensions of meta-atom A down by half, so that it's radius was the same as meta-atom C but it's internal structure was much narrower and had more zig-zag channels. This was done to to observe how this would effect the resonances, with assumption being that they would have a similar profile to meta-atom A, except potentially shifted higher in frequency. From the results in Fig. 5.7, this assumption is immediately shown to be invalid. The scattering coefficients have a much more complicated profile than the other meta-atoms characterised, with potential zero phase crossings corresponding to resonances at 925 Hz in α_0 and 580 Hz in α_1. However, due to the large error in the plots these are tenuous

observations. The main source of error in these results is that the residuals in the scattered field are large; much larger than meta-atom C, even though it has the same radius and angular percentage of the acoustic field recorded. This could be due to the scattered field of the small features in the geometry being more sensitive to reflections and interference in the acoustic measurement apparatus, or that the thinner 0.5 mm wall thickness and small internal channel width tends to transmit low frequency sound which decreases the ability of the mutlipole expansions in (2.49) to accurately represent the acoustic field.

5.3 Summary

The monopole and dipole scattering coefficients of four fabricated meta-atoms were successfully determined using the method from chapter 4. The experimental results of meta-atoms A and B, which had had been previously described in the literature, were found to agree with simulations performed in the papers the meta-atoms were taken from. Error at low frequencies detracted from observed resonances in design A, but design B had excellent agreement. The designs C and D were modified from A and also characterised. Here, the monopolar and dipolar resonances were found to be shifted from the original design, with meta-atom D gaining additional complexities in the profile of it's scattering coefficients.

Chapter 6

Conclusions and Future Work

6.1 Conclusions

This thesis detailed the development of an experimental method to determine the monopole and dipole scattering coefficients of meta-atoms. As the monopolar and dipolar response of meta-atoms have been associated with parameters critical to the design and performance of AMM and metasurfaces, experiemntally determining these scattering coefficients represents a significant step toward realising the potential of AMM to arbitrarily control and structure acoustic fields.

To reach this aim, three main objectives were met. The first of which was to modify an existing acoustic field measurement apparatus in order to accurately record 2D acoustic field data. Chapter 3 described the modifications and testing that was performed on the system during this process. This focussed on removing distortions in the recorded field and minimising interference due to reflections by optimising the anechoic foam edging of the apparatus, adapting the cable management system and microphone control programs to provide accurate positional information, and changing the acoustic source to a small 5 cm diameter loudspeaker to better approximate a point source. Chapter 3 also defined the experimental procedure used to record accurate field data. The second objective was to develop and verify a method of extracting the multipole scattering coefficients from the acoustic data. This was presented in chapter 4. Where, based on the theory of acoustic scattering and multipole expansions outlined in chapter 2, a method using a complex linear fitting of the scattered and incident acoustic field data was described. This method was then verified by extracting the scattering coefficients of a rigid cylinder and comparing them to analytically derived values. The experimental values were found to agree with the analytical, with better agreement seen at higher frequencies above 1000 Hz, where both the small loudspeaker and anechoic foam boundaries of the measurement apparatus have better performance, and the experimental error of the method is decreased. The final objective was to successfully apply this method to meta-atoms, which was the topic of chapter 5. Here two designs already existing in

the literature were characterised. Both of these were experimentally found to have monopolar and dipolar scattering coefficients closely matching simulated values of the resonances taken from the literature. Error at low frequencies somewhat detracted from the results, however higher frequency monopolar resonance above 1000 Hz was found to have excellent agreement with the expected value. Two additional meta-atom designs were also characterised, where these were slightly modified versions of a meta-atom previously tested. Due to the modifications, shifted monopolar and dipolar resonances were also observed.

6.2 Suggestions for Future Work

Suggestions for future work focus mainly on further developing and improving the experimental apparatus and method of determining monopole and dipole scattering coefficients, as well as characterising more advanced meta-atom geometries. As the experimental error in the method decreases at higher frequencies, increasing the cut-off frequency of the acoustic measurement system would provide a larger range of accessible low error acoustic frequencies. This could be done by modifying the microphone gantry arm to allow the microphone belt to sit flush with the bottom of the parallel plate waveguide, such that the two plates can be brought closer together while maintaining the efficacy of the anechoic edging. Another improvement to the apparatus that may decrease measurement error would be to correct the slight bowing in the top parallel plate, however the level of difficulty to do so might be restrictive. The scattering coefficient extraction method could also be further improved by determining the optimal area of an acoustic scan for a given meta-atom size. This would look at the trade-off between reflections from edges and the relative percentage of the angular field recorded, as optimising this may significantly decrease the error seen when characterising a larger meta-atom. Finally, the extraction method could also be extended to experimentally investigate more advanced meta-atom designs. This could look at asymmetrical meta-atoms that couple monopolar and dipolar responses for applications in improved transmissive acoustic metasurfaces.

Bibliography

[1] LAPACK - gelsy. https://software.intel.com/en-us/mkl-developer-reference-c-gelsy.

[2] Banerjee, B., 2011. *An Introduction to Metamaterials and Waves in Composites*. CRC Press/Taylor & Francis Group, Boca Raton, FL. ISBN 978-1-4398-4158-7. OCLC: 861618489.

[3] Beranek, L. L. and Sleeper, H. P., 1946. The Design and Construction of Anechoic Sound Chambers. *The Journal of the Acoustical Society of America*, 18, 1 (Jul. 1946), 140–150. doi:10.1121/1.1916351.

[4] Cheng, Y.; Zhou, C.; Yuan, B. G.; Wu, D. J.; Wei, Q.; and Liu, X. J., 2015. Ultra-sparse metasurface for high reflection of low-frequency sound based on artificial Mie resonances. *Nature Materials*, 14, 10 (Aug. 2015), 1013–1019. doi:10.1038/nmat4393.

[5] Craster, R. V. and Guenneau, S. (Eds.), 2013. *Acoustic Metamaterials: Negative Refraction, Imaging, Lensing and Cloaking*. No. v. 166 in Springer series in materials science. Springer, Dordrecht ; New York. ISBN 978-94-007-4812-5. OCLC: ocn815367245.

[6] Cummer, S. A.; Christensen, J.; and Alù, A., 2016. Controlling sound with acoustic metamaterials. *Nature Reviews Materials*, 1, 3 (Feb. 2016), 16001. doi:10.1038/natrevmats.2016.1.

[7] Diaz-Rubio, A. and Tretyakov, S. A., 2017. Perfect acoustic metasurfaces. *arXiv:1702.05872 [cond-mat, physics:physics]*, (Feb. 2017).

[8] Engheta, N.; Ziolkowski, R. W.; and Institute of Electrical and Electronics Engineers (Eds.), 2006. *Metamaterials: Physics and Engineering Explorations*. Wiley-Interscience, Hoboken, N.J. ISBN 978-0-471-76102-0. OCLC: ocm61757037.

[9] Haberman, M. R., 2016. Acoustic Metamaterials. *Acoustics Today*, 12, 3 (2016), 31–39.

[10] Hawkes, P. W., 2011. *Advances in Imaging and Electron Physics*. Academic Press, Amsterdam. ISBN 978-0-12-385861-0. OCLC: 840443151.

[11] Haynes, W. M.; Lide, D. R.; and Bruno, T. J., 2016. *CRC Handbook of Chemistry and Physics a Ready-Reference Book of Chemical and Physical Data*. ISBN 978-1-4987-5429-3. OCLC: 973005399.

[12] Kang, Y. J. and Bolton, J. S., 1996. Optimal Design of Acoustical Foam Treatments. *Journal of Vibration and Acoustics*, 118, 3 (1996), 498. doi:10.1115/1.2888212.

[13] Krowne, C. M. and Zhang, Y. (Eds.), 2007. *Physics of Negative Refraction and Negative Index Materials: Optical and Electronic Aspects and Diversified Approaches*. No. 98 in Springer series in materials science. Springer, Berlin ; New York. ISBN 978-3-540-72131-4.

[14] Krushynska, A. O.; Bosia, F.; Miniaci, M.; and Pugno, N. M., 2017. Tunable spider-web inspired hybrid labyrinthine acoustic metamaterials for low-frequency sound control. *arXiv:1701.07622 [cond-mat]*, (Jan. 2017).

[15] Li, Y.; Jiang, X.; Li, R.-q.; Liang, B.; Zou, X.-y.; Yin, L.-l.; and Cheng, J.-c., 2014. Experimental Realization of Full Control of Reflected Waves with Subwavelength Acoustic Metasurfaces. *Physical Review Applied*, 2, 6 (Dec. 2014). doi:10.1103/PhysRevApplied.2.064002.

[16] Liu, Z.; Zhang, X.; Mao, Y.; Zhu, Y. Y.; Yang, Z.; Chan, C. T.; and Sheng, P., 2000. Locally Resonant Sonic Materials. *Science*, 289, 5485 (Sep. 2000), 1734–1736. doi:10.1126/science.289.5485.1734.

[17] Lu, G.; Ding, E.; Wang, Y.; Peng, X.; Cui, J.; Liu, X.; and Liu, X., 2017. Realization of acoustic wave directivity at low frequencies with a subwavelength Mie resonant structure. *Applied Physics Letters*, 110, 12 (Mar. 2017), 123507. doi:10.1063/1.4979105.

[18] Ma, G. and Sheng, P., 2016. Acoustic metamaterials: From local resonances to broad horizons. *Science Advances*, 2, 2 (Feb. 2016). doi:10.1126/sciadv.1501595.

[19] Main, I. G., 1984. *Vibrations and Waves in Physics*. Cambridge University Press, Cambridge [Cambridgeshire] ; New York, 2nd ed edn. ISBN 978-0-521-26124-1 978-0-521-27846-1.

[20] Mei, C. C., 1997. *Mathematical Analysis in Engineering: How to Use the Basic Tools*. Cambridge University Press, Cambridge. ISBN 978-0-521-58798-3. OCLC: 833191409.

[21] Meyer, E. and Neumann, E.-G., 1972. *Physical and Applied Acoustics: An Introduction*. Academic Press. Google-Books-ID: BavvAAAAMAAJ.

[22] Muhlestein, M. B., 2016. *Willis Coupling in Acoustic and Elastic Metamaterials*. Ph.D. thesis, University of Texas at Austin.

[23] Shen, C., 2016. *Design of Acoustic Metamaterials and Metasurfaces*. Ph.D. thesis, North Carolina State University, Raleigh, North Carolina.

[24] Solymar, L. and Shamonina, E., 2009. *Waves in Metamaterials*. Oxford University Press, Oxford ; New York. ISBN 978-0-19-921533-1. OCLC: ocn245558989.

[25] Stefan Punzet, 2016. Design and construction of an Acoustic Scanning Stage. Technical report, Australian National University, Canberra, A.C.T.

[26] Strutz, T., 2011. *Data fitting and uncertainty: a practical introduction to weighted least squares and beyond*. Vieweg + Teubner, Wiesbaden. ISBN 978-3-8348-1022-9. OCLC: 845641143.

[27] Xie, B.; Tang, K.; Cheng, H.; Liu, Z.; Chen, S.; and Tian, J., 2017. Coding Acoustic Metasurfaces. *Advanced Materials*, 29, 6 (Feb. 2017), 1603507. doi:10.1002/adma.201603507.

[28] Xie, Y.; Wang, W.; Chen, H.; Konneker, A.; Popa, B.-I.; and Cummer, S. A., 2014. Wavefront modulation and subwavelength diffractive acoustics with an acoustic metasurface. *Nature Communications*, 5 (Nov. 2014), 5553. doi:10.1038/ncomms6553.

[29] Zhao, J., 2016. *Manipulation of Sound Properties by Acoustic Metasurface and Metastructure*. Springer Theses. Springer Singapore, Singapore. ISBN 978-981-10-2124-4 978-981-10-2125-1. doi:10.1007/978-981-10-2125-1.

[30] Zigoneanu, L., 2013. *Design and Experimental Applications of Acoustic Metamaterials*. Ph.D. thesis, Duke University.

[31] Zigoneanu, L.; Popa, B.-I.; and Cummer, S. A., 2011. Design and measurements of a broadband two-dimensional acoustic lens. *Physical Review B*, 84, 2 (Jul. 2011), 024305. doi:10.1103/PhysRevB.84.024305.